Super-Resolution Mid-Infrared Spectro-Microscopy of Biological Applications through Tapping Mode and Peak Force Tapping Mode Atomic Force Microscope

Haomin Wang ¹¶, Qing Xie ²¶, and Xiaoji G. Xu ^{2*}

- ¹: Division of Chemistry and Chemical Engineering, California Institute of Technology, Pasadena, CA 91125, USA
- ²: Department of Chemistry, Lehigh University, Bethlehem, PA 18015, USA
- *: Corresponding email: xgx214@lehigh.edu
- 1: These authors contributed equally

Table of Contents

Abstract	2
Keywords	2
Abbreviations	2
I. Introduction	2
2. Methods	5
2.1 Scattering-type scanning near-field optical microscopy (s-SNOM)	5
2.2 Photo-induced force microscopy (PiFM)	6
2.3 Peak force infrared (PFIR) microscopy	7
3. Applications	10
3.1 s-SNOM in plant biology	10
3.2 s-SNOM in the characterization of virus, fungi, and bacteria	12
3.3 s-SNOM in the characterization of cells and tissues	13
3.4 s-SNOM in the characterization of biomolecules	15
3.5 s-SNOM in assisting biomaterial engineering	
3.6 s-SNOM in the aqueous phase	18
3.7 PiFM in biological applications	19
3.8 PFIR in biological applications	21
4. Summary and outlook	23
Acknowledgments	24
References	24

Abstract

Small biomolecules at the subcellular level are building blocks for the manifestation of complex biological activities. However, non-intrusive *in situ* investigation of biological systems has been long daunted by the low spatial resolution and poor sensitivity of conventional light microscopies. Traditional infrared (IR) spectro-microscopy can enable label-free visualization of chemical bonds without extrinsic labeling but is still bound by Abbe's diffraction limit. This review article introduces a way to bypass the optical diffraction limit and improve the sensitivity for mid-IR methods – using tip-enhanced light nearfield in atomic force microscopy (AFM) operated in tapping and peak force tapping modes. Working principles of well-established scattering-type scanning near-field optical microscopy (s-SNOM) and two relatively new techniques, namely, photo-induced force microscopy (PiFM) and peak force infrared (PFIR) microscopy, will be briefly presented. With ~10-20 nm spatial resolution and monolayer sensitivity, their recent applications in revealing nanoscale chemical heterogeneities in a wide range of biological systems, including biomolecules, cells, tissues, and biomaterials, will be reviewed and discussed. We also envision several future improvements of AFM-based tapping and peak force tapping mode nano-IR methods that permit them to better serve as a versatile platform for uncovering biological mechanisms at the fundamental level.

Keywords

Mid-IR super-resolution microscopy, Near-field light-matter interaction, s-SNOM, PiFM, PFIR microscopy, In situ bioimaging, Cell biology

Abbreviations

STED: Simulated emission depletion; PALM: Photo-activated localization microscopy; STORM: Stochastic optical reconstruction microscopy; IR: Infrared; AFM: Atomic force microscopy; PTIR: Photothermal induced resonance; SNOM: Scanning near-field optical microscopy; NSOM: Near-field scanning optical microscopy; s-SNOM: Scattering-type scanning near-field optical microscopy; PiFM: Photo-induced force microscopy; PFIR: Peak force infrared; SPM: Scanning probe microscopy; SNOM: Scanning near-field optical microscopy; CW: Continuous wave; QCL: Quantum cascade laser; FTIR: Fourier transform infrared spectroscopy; DFG: Difference frequency generation; Q-factor: Quality factor; PFT: Peak force tapping; DAQ: Data acquisition; FFT: Fast Fourier transform; PeakForce ONM: Peak force quantitative nano mechanical characterization; OPO: Optical parametric oscillator; TMV: Tobacco mosaic virus; Galf: Galactofuranose; E. coli: Escherichia coli; RBC: Red blood cell; CLSM: Confocal laser scanning microscopy; DPPC: 1,2-dipalmutiyl-sn-glycero-3-phosphocholine; DSPC: 1,2-distearoyl-snglycero-3-phosphocholine; DMPC: 1,2-dimyristoyl-sn-glycero-3-phosphocholine; UV: Ultraviolet; GB: Gigabyte; PEG: Poly(ethylene glycols); AuNP: Gold nanoparticle; PCA: Principal component analysis; ATR-FTIR: Attenuated total reflection Fourier transform infrared spectroscopy; CFM: Chemical force microscopy; LiPFIR: Liquid-phase peak force infrared microscopy; SEM: Scanning electron microscopy; HS-AFM: High speed AFM

I. Introduction

Living systems are composed of various hierarchical biological organizations, which play crucial roles in maintaining life activities in a wide range of length scales ranging from: the body level, the tissue level (> $100 \mu m$), the cellular/subcellular level ($0.1 - 100 \mu m$), down to the molecular level ($\sim 1 nm$) [1, 2]. Below the cellular level, numerous small molecules and biomacromolecules co-exist and interact with each other

and organelles, leading to orderly yet complicated manifestations of biological activities. For example, small amino acid molecules are synthesized at ribosomes to become functional proteins through transcription and translation, processes that are regulated by a series of enzymes [3]. Fundamental knowledge at the subcellular level is pivotal for obtaining a comprehensive picture of how living systems work, thus will contribute to the discovery of drug mechanisms and new therapeutic pathways.

Fluorescence microscopy is widely used to specifically label and map components of interest to get *in situ* information at the subcellular level non-intrusively [4]. The illumination and detection paths in fluorescence microscopy are both far-field, indicating the spatial resolution is usually diffraction-limited [5, 6]. To achieve super-resolution fluorescence imaging with sub-wavelength resolution, different approaches have been developed to resolve the point spread function of fluorophores more precisely. Stimulated emission depletion (STED) microscopy [7], photo-activated localization microscopy (PALM) [8], and stochastic optical reconstruction microscopy (STORM) [9] are three successful implementations of such techniques. Although the spatial resolution could be improved to < 100 nm with these methods, several intrinsic limits still hinder far-field fluorescence microscopy. For instance, many biomolecules are naturally nonfluorescent. Imaging these molecules requires fluorescent labels to be molecular-specific and low-profile so that the physicochemical properties of labeled molecules are not altered after labeling. It is hard to achieve such requirements simultaneously for small biomolecules such as nucleotides, amino acids, fatty acids, choline, glucose, and drugs [1, 2].

The limitations of fluorescence microscopy are lifted in infrared (IR) spectro-microscopy. Absorption fingerprints in the mid-IR region are unique for each molecule and extensively used for chemical identification and characterization [10]. In IR spectro-microscopies, vibrational levels of molecules are probed directly. Thus, no additional labels are required. Besides, IR bands are usually narrower than fluorescence emission bands, allowing for the unambiguous identification of multiple chemical compositions. However, the longer wavelengths of IR render the spatial resolution of far-field IR methods much worse than that of fluorescence microscopy [11]. Although several super-resolution IR microscopies have developed spatial resolution comparable to traditional fluorescence microscopy using photothermal [12, 13] or photoacoustic detections [14], the spatial resolution is still diffraction limited by the wavelength of detected photons and far from nanoscale imaging needs.

To improve the spatial resolution well below the far-field diffraction limit, one can exploit near-field illumination. A popular way to achieve near-field illumination is to make use of the sharp metallic or metal-coated tip in an atomic force microscope (AFM) [15-18]. When placed under far-field illumination, an enhanced and highly localized light nearfield will form around the tip apex due to plasmonic enhancement [19]. The formed near-field hotspot with a size comparable to the tip radius (usually 20 - 30 nm) can serve

as a nanoscale illumination source and achieve wavelength-independent spatial resolutions of only tens of nanometers, depending only on the tip apex geometry. This near-field illumination strategy has been successfully incorporated with a series of AFM working modes, including contact mode, tapping mode, and peak force tapping mode. In these modes, nano-IR imaging is performed by raster scanning the tip over the sample while registering the near-field IR signal. Nano-IR spectroscopy is achieved by positioning the tip at the location of interest and registering the IR signal while sweeping the IR frequency or using a broadband light source with Fourier transform IR techniques.

Compared with traditional IR methods, AFM-based nano-IR techniques have at least two advantages in investigating biological samples: 1, the high spatial resolution, which routinely enables cellular and subcellular-level studies; 2, the high sensitivity brought by the strong tip-enhancement, which is must-needed in detecting biomolecules and drug molecules with low concentrations. Photothermal induced resonance (PTIR), one of the most widely applied AFM-IR methods based on contact mode AFM, was developed by Alexandre Dazzi and colleagues around 2005 [20]. In PTIR, pulsed IR laser is focused into the tip-sample region, and the deflection of the cantilever measures the photothermal expansion. As one of the first few nanoscopic IR methods, PTIR has yielded a multitude of applications ranging from polymer characterization, photovoltaics, plasmonics, and life sciences [16]. However, traditional PTIR technique with contact mode requires the AFM tip always to contact the sample, limiting the spatial resolution and making it prone to sample scratch due to lateral forces. Thus, unless avoid using the AFM contact mode (such as in the tapping AFM-IR method, see Section 2.2), traditional PTIR technique is not suitable for delicate specimens such as bio membranes or samples with rough and sticky surfaces [18].

Besides the contact mode, AFM can also operate in tapping mode [21] and peak force tapping mode (also known as the pulsed force mode) [22, 23]. These two modes are known to be less demanding in sample selection and can better preserve both the tip and sample surface during AFM scans than the contact mode. Therefore, nano-IR methods based on these two modes of AFM are more suitable for most small and delicate biological and pharmaceutical samples. In this review article, a total of three AFM-based superresolution IR spectro-microscopies, including scattering-type scanning near-field optical microscopy (s-SNOM), photo-induced force microscopy (PiFM), and peak force infrared (PFIR) microscopy, will be introduced and discussed. These methods are based on tapping mode and peak force tapping mode. We will begin with a brief introduction of the working principle for each technique. Following their recent applications in biological studies, we provide a summary and an outlook of the future technical and methodological developments on how these methods could better assist biological and pharmaceutical studies.

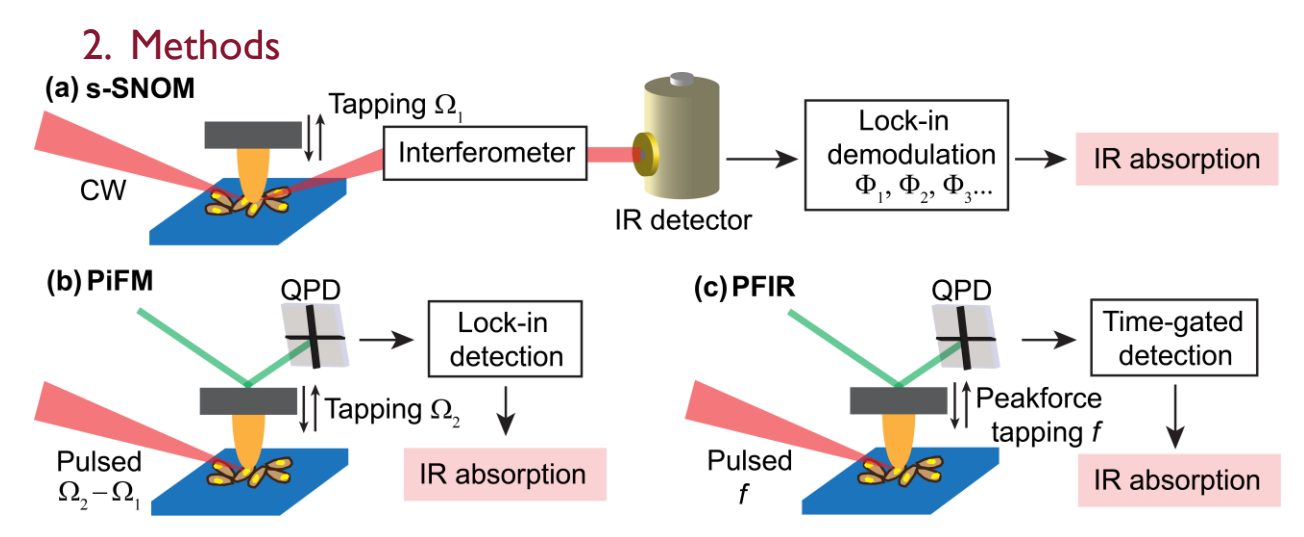


Figure 1. Simplified experimental setups of s-SNOM (a), PiFM (b), and PFIR microscopy (c). CW: Continuous wave; QPD: Quadrant photodiode; Φ: Demodulated near-field phase; Ω: Mechanical resonance frequency of the cantilever, $\Omega_2 \approx 6.3\Omega_1$; f: Peak force tapping frequency.

2.1 Scattering-type scanning near-field optical microscopy (s-SNOM)

The invention of scanning probe microscopy (SPM) in the 1980s [24] had significantly enhanced the research tool to access the nanoscale. Many efforts have been made to bypass the diffraction limit of light microscopy through combining optical methodologies with SPM. Scanning near-field optical microscopy (SNOM, or near-field scanning optical microscopy, NSOM) based on a small aperture was one of the early inventions of optical SPM and is still a powerful technique in biological applications [25, 26]. However, the resolution of aperture-based SNOM is bound to about λ 10 due to the lower limit of optical aperture size [27]. In contrast, modern scattering-type SNOM (s-SNOM), first pioneered by A. Claude Boccara and coworkers around 1995 [28, 29], and fully developed by Fritz Keilmann, Rainer Hillenbrand, and others, takes advantage of metal-coated tips in AFM and achieve a much higher wavelength-independent spatial resolution of 20 – 30 nm [30, 31]. Such a high resolution is essential in imaging subcellular targets and deciphering in-depth biological mechanisms.

In s-SNOM, generally, a continuous-wave (CW) IR laser beam is focused onto the tip-sample region of an AFM (**Figure 1a**). Pulsed laser sources are also employed in some s-SNOM applications [32, 33] but are not widely applied in bio-relevant studies. The metal-coated tip acts as a nanoscale antenna, confining the incoming IR field into a small focal volume and generating a hotspot for localized illumination. As the cantilever oscillates vertically in AFM tapping mode, the tip-sample distance also oscillates periodically in a harmonic fashion. The scattered light from the tip-sample region is then sent to a far-field IR detector with interferometric detection schemes (e.g., homodyne [34] and pseudo heterodyne [35]) enabled by a Michelson interferometer. As a result, the detected light scattering also fluctuates at the tapping frequency of Ω_1 (usually the first mechanical resonance frequency of cantilever, ranging from several tens to hundreds

of kHz). The fluctuating electric signal from IR detector is routed into a lock-in amplifier, which demodulates the compound signal at a series of tapping harmonics Ω_1 , $2\Omega_1$, $3\Omega_1$,... Because s-SNOM uses the interferometric detection, both demodulated amplitudes $(A_{\Omega_1}, A_{2\Omega_1}, A_{3\Omega_1}, ...)$ and phases $(\Phi_{\Omega_1}, \Phi_{2\Omega_1}, \Phi_{3\Omega_1}, ...)$ can be extracted. The main far-field background from the tip-sample region is mostly contained in the first harmonic component [36, 37] and thus is effectively removed in higher harmonic signals. The higher harmonic signals (the anharmonicities) represent the near-field modulation to the optical scattering, which are indicative of the near-field tip-sample polarizability and used as s-SNOM signal.

The amplitude and phase information from s-SNOM are functions of local complex dielectric properties. Therefore, s-SNOM imaging has been extensively used in fields where the nanoscale light field distribution needs to be resolved. For instance, s-SNOM with monochromatic IR sources (e.g., quantum cascade laser, QCL) is widely applied in imaging polaritons in plasmonic or dielectric materials, especially in two-dimensional materials, including graphene, boron nitride, and transition metal dichalcogenides [38]. Subwavelength electromagnetic field imaging of artificial plasmonic nanostructures (e.g., gold antennas) and materials with mesoscopic properties (e.g., vanadium dioxide) are another areas where s-SNOM has played important roles in monitoring phase transitions and discovering new physics [39].

On the other hand, s-SNOM is capable of chemical imaging because the near-field optical phase signal is correlated to IR absorptions. Combining s-SNOM with a broadband light source, nano-FTIR absorption spectroscopy with 20-nm spatial resolution could be implemented [40]. On a variety of samples including polymers, biomaterials, biomolecules, and cells, spectra measured from nano-FTIR are found to correspond well with far-field FTIR spectra. Nano-FTIR with broadband light sources (e.g., IR difference-frequency generation, DFG) also enables hyperspectral chemical imaging, providing rich information in both spatial and spectral dimensions in one single AFM scan. Recently, the adoption of total reflection illumination has enabled s-SNOM to be compatible with liquid environments [41-43], which opens the possibility of spatiotemporally characterizing and monitoring physicochemical transformations of biological systems in native states *in vivo*.

2.2 Photo-induced force microscopy (PiFM)

In 2016, PiFM was introduced into the nano-IR community by its inventor Kumar H. Wickramasinghe and coworkers in Molecular Vista [44]. PiFM operates in a modified AFM tapping mode, where a high quality factor (Q-factor) cantilever is driven at its second mechanical resonance frequency Ω_2 , which is about six times higher than the first mechanical eigenmode Ω_1 used in regular tapping mode and s-SNOM. Unlike s-SNOM, PiFM uses a pulsed laser source with a tunable repetition rate that matches the frequency difference of $\Omega_2 - \Omega_1$, achieving sideband excitation and force heterodyne detection [45]. The photo-induced force exerted onto the cantilever is measured as the signal through the quadrant photodiode of AFM, eliminating

the need to detect light scattering as in s-SNOM. At absorbing wavelengths, the tip tapping frequency of Ω_2 and the pulse repetition rate of $\Omega_2 - \Omega_1$ together generate cantilever oscillations at a sideband frequency of Ω_1 , which coincides with the cantilever's first mechanical eigenmode. Therefore, the IR-induced force signal at Ω_1 is amplified further. On the contrary, the background is primarily from periodical photothermal excitation of the AFM cantilever at $\Omega_2 - \Omega_1$, which diminishes at Ω_1 . With this innovative force heterodyne design, IR PiFM has been demonstrated to reach < 10 nm spatial resolution on a range of samples and superb surface sensitivity on self-assembled monolayers [46]. The origin of the photo-induced force was initially thought to be from tip-induced dipole-dipole interactions [47, 48]. However, a series of detailed examinations later have shown that the photothermal expansion also contributes to the detected signal [49-52]. The detected photo-induced force might be a mixture of both induced dipole interactions and photothermal expansion.

Another variant of tapping mode AFM-IR (tapping AFM-IR) was introduced around 2018 by Anasys (now a part of Bruker) to enhance the PTIR techniques [53, 54]. Like PiFM, tapping AFM-IR uses pulsed IR excitation and heterodyne force detection. The tapping amplitude is often modified in tapping AFM-IR to ensure the maximal tip-sample interaction so that the photothermal expansion can be read out more efficiently. To alleviate the problem caused by the cantilever frequency drift during the hard tapping, a phase lock loop can be implemented to account for the drift of Ω_1 and Ω_2 on the fly. Tapping AFM-IR has been utilized to acquire nano-IR images of drug-related molecules, including paclitaxel distribution in lipid-polymer membranes [54], chemotherapeutic drug-loaded liposomal nanocarriers [55], drug-loaded polymeric nanoparticles [53], and drug/metal monolayers [56].

2.3 Peak force infrared (PFIR) microscopy

The interaction volume between the tip and sample is minimized in tapping mode, thus tapping AFM has higher spatial resolution than the contact mode. However, tapping mode is unable to straightforwardly obtain mechanical information from the sample, such as modulus and deformation. Peak force tapping (PFT) mode, also known as the pulsed force mode [22, 23], fills the gap between the contact mode and the tapping mode AFM. In PFT mode, the tip-sample distance oscillates at a low frequency of f(e.g., 1-8 kHz). Within each PFT cycle, the tip is brought into contact with the sample and then retracted when the cantilever deflection reaches a threshold. The threshold force exerted on the cantilever in each PFT cycle, named peak force, is maintained constant as the feedback setpoint. During each tapping cycle, a force curve vs. tip-sample distance is obtained with two regions: tip-sample in-contact and out-of-contact regions. Therefore, PFT mode combines advantages from both contact and tapping mode. Like contact mode, the mechanical information of sample surface (e.g., modulus and adhesion) can be extracted from the in-contact force curves. Similar to tapping mode, the contact time between the tip and sample is maintained small by setting

a small peak force to achieve minor tip wearing, reduced sample damage, and higher spatial resolution. PFT mode has been demonstrated as a robust and versatile AFM mode in both air and liquid conditions [57-61].

Based on PFT mode, the PFIR microscopy was developed by our group in 2017 [62]. The experimental setup of PFIR is shown in Figure 1c. The laser in PFIR is pulsed and synchronized with the PFT at a much lower frequency of f (1 – 8 kHz) than the cantilever mechanical resonance frequency and the difference frequency used in PiFM ($\Omega_2 - \Omega_1$). Therefore, time-gated detection triggered by the same frequency f is preferred by commercially available data acquisition (DAQ) devices over a lock-in amplifier. The arrival time of IR pulses at each PFT cycle is adjusted to be right after the maximal cantilever deflection (the peak force point) to not disturb the PFT feedback. To enhance the sensitivity, one can use a train of IR pulses with the repetition rate matching one of the cantilever's mechanical resonances instead of a single pulse [63]. At IR absorbing frequency, the rapid photothermal expansion of the sample mechanically excites the cantilever, i.e., through a kick, causing the cantilever to oscillate. Such oscillations persist according to the Q-factor of the cantilever. The AFM quadrant photodiode can directly read out the instant photothermal expansion. The extra oscillations (ringdowns) induced by photothermal expansion detected by the DAQ are sent through the fast Fourier transform (FFT) in real-time to extract the oscillation amplitude. The instant photothermal expansion and the oscillation amplitude of ringdowns compose two signal channels used in PFIR, and the latter is more often used in imaging and spectroscopy.

Since its invention, PFIR microscopy with 6-10 nm spatial resolution has been applied over various samples, including polymers [62], aerosol particles [64], boron nitride nanotubes and flakes [63, 65], yeast cell walls [66], natural fibrous woods [67], shell rocks [68] and perovskites [69, 70]. Liquid-phase PFIR has also been developed using the total internal reflection scheme [65, 71, 72]. Besides, additional mechanical information, such as modulus and adhesion, is captured simultaneously with IR signal in PFIR through the built-in function of PeakForce quantitative mechanical characterization (PeakForce QNM), enabling multichannel imaging and nanoscale investigations on correlative mechanical and optical properties.

Some technical parameters of s-SNOM, PiFM, and PFIR are summarized in Table 1.

Table 1. Comparison between s-SNOM, PiFM, and PFIR

	s-SNOM	PiFM	PFIR
AFM mode	Tapping at Ω_1	Tapping at Ω_2	Peak force tapping/pulsed force mode
Mid-IR light source	QCL, gas laser, broadband DFG, synchrotron radiation, plasma	QCL, OPO	QCL, OPO
Laser source repetition rate	CW or high repetition rate $> 10^6 \text{ Hz}$	$10^5\!\sim10^6Hz$	$\sim 10^3 \ Hz$
Detection scheme	Light detection + lock-in demodulation	Force detection + lock-in detection	Force detection + time- gated detection
Typical resolution	20 – 30 nm	~ 10 nm	~ 10 nm
Complimentary mechanical property	Not available	Not available	Quantitative and direct by PeakForce QNM

3. Applications

3.1 s-SNOM in plant biology

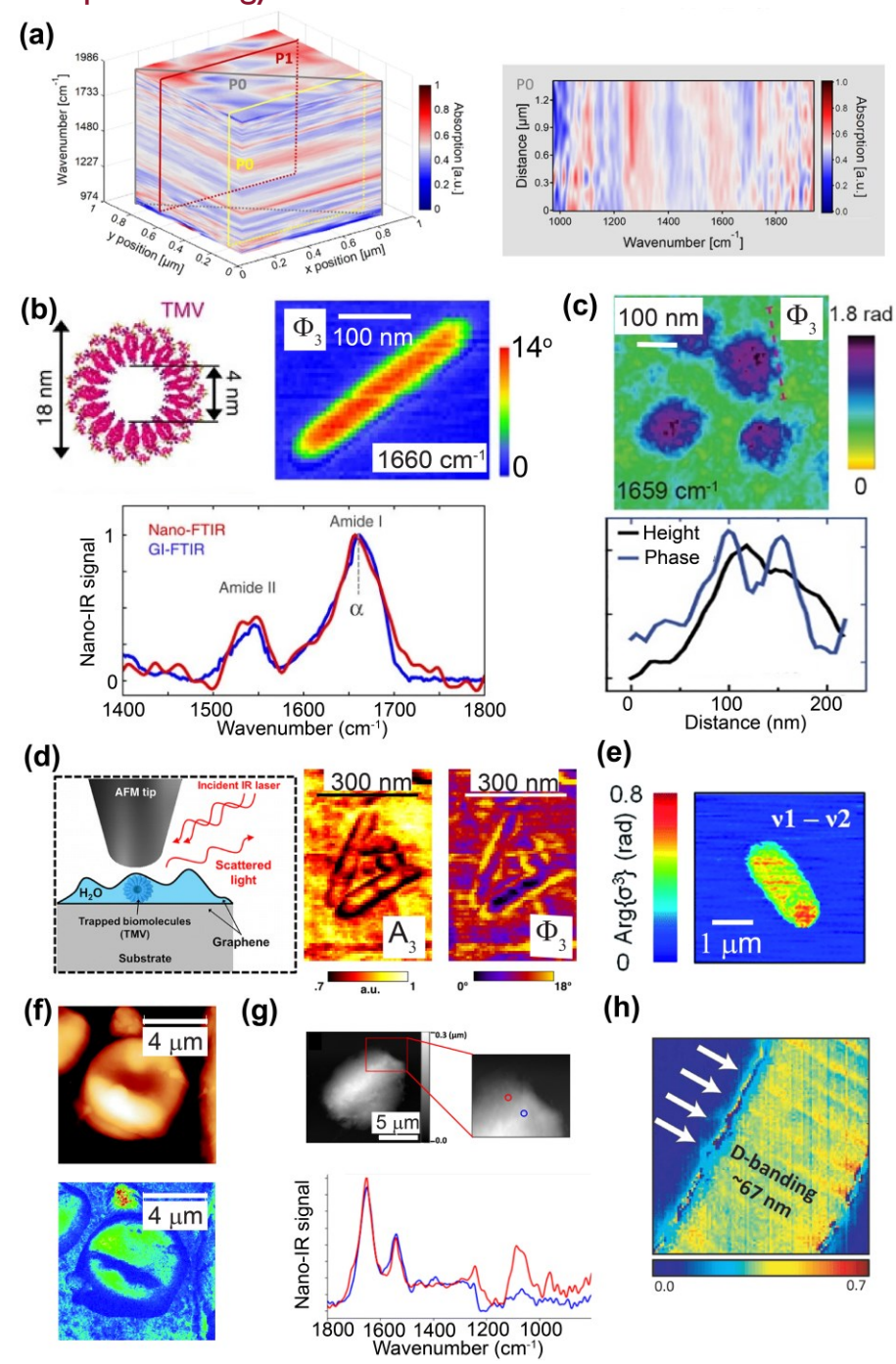


Figure 2. s-SNOM in resolving biological systems. (a) Hyperspectral near-field phase cube obtained from a $1\times1~\mu\text{m}^2$ area of plant cell walls. A cross-sectional profile along the plane P0 (gray) is shown to the right. Adapted from ref. [73] with permission. (b) A schematic of the dimension of TMV and its near-field phase image from the third harmonic (Φ_3) at 1660 cm⁻¹. The Near-field phase spectrum obtained from the TMV (red) overlaid with the FTIR spectrum collected from the

ensemble (blue) is shown at the bottom. Adapted from ref. [74] with permission. (c) s-SNOM Φ_3 image of influenza virus X31 at 1659 cm⁻¹. The line profile across the red dashed line in the image is plotted at the bottom and overlaid with AFM height, revealing hemagglutinin protrusions on the virus membrane. Adapted from ref. [75] with permission. (d) Illustration of the s-SNOM liquid cell based on monolayer graphene (left panel). The right panel shows third harmonic amplitude (A₃) and phase (Φ_3) images under 890 cm⁻¹ for individual TMVs. Adapted from ref. [76] with permission. (e) s-SNOM difference frequency image of a single E. coli. The image was the difference between 1660 cm⁻¹ (amide I) and 1710 cm⁻¹ (background artifacts), indicating proteins are distributed homogeneously across the E. coli. Adapted from ref. [77] with permission. (f) AFM topography and s-SNOM Φ_3 image of a single human blood cell in a biopsy. Adapted from ref. [78] with permission. (g) AFM topography of a human lymphocyte nucleus. Nano-FTIR spectra from denoted locations in the topography are plotted at the bottom. In addition to amide I & II bands, the thinner region spectrum (red) shows DNA absorption bands within 1000 – 1200 cm⁻¹. Adapted from ref. [79] with permission. (h) s-SNOM absorption image of the bovine tail tendon. The D-band pattern with spacings of ~ 67 nm is clearly resolved. Adapted from ref. [80] with permission.

The nanoscale spatial resolution of s-SNOM allows revealing chemical distribution in plant structures in unprecedented detail with rich chemical information. Pereira *et al.* combined s-SNOM with ultra-broadband synchrotron radiation to spectroscopically analyze chemical components of pit membranes [81], which play essential roles between water-conducting vessels in the xylem of angiosperm plants. IR signatures of lignin, phenolic compounds, cellulose, pectin, and proteins were located and compared between inter-vessel pit membrane, vessel-parenchyma pit membrane, and developing cell wall. Their spectroscopic findings with s-SNOM were further corroborated by parallel AFM-IR imaging and spectroscopy results, suggesting the chemistry in pit membranes is more complicated than previously thought. In another work, Zancajo *et al.* utilized s-SNOM to track biominerals of silica in both fixed and unfixed plant cells and tissues [82]. The amount of silica was found to vary spatially from the most silicified papilla, less silicified sclerenchyma cells, to no silicified cell walls of the xylem tissue in wheat awns. In addition, the authors demonstrated that nano-FTIR spectra could also be collected from native plant tissues without further substrate enhancement. These findings pave the way for using s-SNOM to investigate inorganic-organic hybrid biomaterials *in situ.*

Recently, *in situ* hyperspectral imaging of plant cell walls was demonstrated by Charrier *et al.* [73]. Data cubes including mechanical tapping phase, near-field amplitude (reflectivity), and near-field phase (absorption) were acquired from a $1 \times 1 \mu m^2$ area of plant cell walls of *Populus Nigra* wood (**Figure 2a**). The multi-channel hyperspectral data allow for the revelation of correlative mechanical, optical and chemical relationships at the nanoscale. Two major chemical components of cellulose and lignin were identified and located in plant cell walls. The authors also used s-SNOM as a characterization tool to monitor the efficiency of a delignification process, a three-step chemical extraction process developed to extract lignin biomass from woods. From hyperspectral images at each treatment step, lignin contents in plant cell walls were found to be decreased. However, the lignin removal was not complete due to the low

solubility of high molecular weight lignin in the acetylation step, suggesting that pretreatment is necessary for increasing the delignification efficiency. Moreover, the nanoscale distribution of dielectric constants (refractive index n and extinction coefficient k) of the sample was calculated from the hyperspectral data cube. The (n, k) variations were proved to be dependent on chemical environments, indicating that s-SNOM could be a powerful tool in developing plant-based meta-materials.

3.2 s-SNOM in the characterization of virus, fungi, and bacteria

The high spatial resolution of s-SNOM combined with nano-FTIR capability has opened the door for diverse cellular and subcellular-level investigations on small viruses, fungi, and bacteria specimens. For nano-IR inspection of the virus, Amenabar *et al.* first showed the characterization of tobacco mosaic virus (TMV) with s-SNOM nano-FTIR (**Figure 2b**) [74]. Near-field IR spectra obtained from a single TMV correlate well with FTIR spectra obtained from the ensemble sample, both showing amide I and II absorptions. Gamage *et al.* have shown that s-SNOM can be used to track structural and chemical alterations during environmental pH changes of a single enveloped virus, influenza X31 (**Figure 2c**) [75]. For an enveloped virus to infect targets, it was previously postulated that a targeting membrane must be present nearby to trigger the virial fusion. However, the authors found when exposed to lower pH environments, deformations of virus particles could still occur even without the presence of a targeting membrane. During the structural deformation, s-SNOM images at protein absorption and phosphate absorption suggested protein distributions across the virus were uniform. At the same time, the lipids and RNA components were more fragmented distributed. Moreover, the authors confirmed in the single virus level that the treatment of fusion inhibitor molecules could prevent virus membranes from being disrupted in acid environments. These experimental results are inspiring for developing new mechanisms for blocking viral entry into cells.

To date, most s-SNOM applications have been performed in air and dried conditions. This is due to the technical difficulty of delivering and detecting mid-IR light through the strongly absorbing water medium. To overcome this limitation, in 2015, Khatib *et al.* reported a graphene-based platform for s-SNOM characterization of individual TMVs [76]. The enclosure composed of large-area graphene monolayer was filled with virus and water, thus allowing for investigating IR signatures of single virion in the native environment with regular s-SNOM operations in the air (**Figure 2d**). Water absorption and amide I and II bands of TMV were resolved through both near-field imaging and spectroscopy, demonstrating the capability of s-SNOM to examine biomacromolecules in aqueous conditions. However, implementing the thin graphene monolayer in this work is not routinely feasible. More technological developments are needed for s-SNOM to be fully compatible with general samples in liquids.

Joined by other modalities, s-SNOM has been participating in fungi and bacteria research as a superresolution chemical resolving tool to reveal nanoscale chemical heterogeneities. Bakir *et al.* have used sSNOM with synchrotron radiation to obtain mid-IR spectra from specific points on single fungi cells of *Aspergillus nidulans* [83]. In addition to architecture alterations of two gene deletion strains compared to the wild type *A. nidulans*, compositional changes were also discovered by a series of near-field spectra. It was found that gene deletion strains that lack the galactofuranose (Galf) exhibit less β-glucan but more α-glucan on the ultrastructure of cell walls, which underscored the importance of Galf in maintaining the integrity and biofunction of fungi cell walls. For bacteria imaging, sample preparation protocols of general bacterial samples were reported, and a total of 15 bacterial species had been imaged by s-SNOM [84]. Another study conducted by Birarda *et al.* utilized s-SNOM nano-FTIR to track biofilm growth produced by a clinical strain of *Klebsiella pneumoniae* [85]. In addition to confocal and diffraction-limited IR spectroscopy, nano-FTIR resolved nanoscale chemical distributions in detail on the surface of the grown biofilm. Recently, a systematic spectroscopic investigation in the metal hydride chemistry of [FeFe]-hydrogenase was conducted in genetically edited *Escherichia coli* (*E. coli*) cells under whole-cell conditions [77]. In this work, s-SNOM nano-FTIR assisted in monitoring the integrity of individual cells based on amide I absorption of proteins (**Figure 2e**).

3.3 s-SNOM in the characterization of cells and tissues

Cells are composed of complex environments with rich chemical contents. Spatially resolving chemical heterogeneities in such complex systems without extrinsic labeling is highly desirable for biological and pharmaceutical research. Red blood cells (RBCs) are one of the first biological cells studied by s-SNOM. s-SNOM imaging was demonstrated on a single RBC in 2016 (**Figure 2f**) [78]. Later, Tranca *et al.* obtained nanoscale complex refractive indices of human erythrocytes based on s-SNOM imaging and a dipole model [86]. Moreover, a systematic spectroscopic analysis of isolated and intact RBC membranes was carried out by Blat *et al.* [87]. On the intact RBC cell, s-SNOM nano-FTIR was shown to reliably reproduce IR signatures of protein conformational changes of both healthy and diseased RBC membranes, comparable to the FTIR results obtained from isolated RBC membranes. With a small penetration depth of ~20 nm [88], s-SNOM can serve as an excellent method for surface characterization without the need to isolate surface structures such as bio-membranes.

In a study of biochemical properties of human acidophilic granulocytes (eosinophils), near-field spectra from s-SNOM were able to identify slight variations of protein secondary structures on the surface of the eosinophilic leukemia cell line [89]. In another study, human lymphocytes' nuclei were spectroscopically inspected by s-SNOM with both synchrotron radiation and broadband DFG sources [79]. IR signatures of protein, DNA, hydrocarbon, ribose, and phosphate in the nucleus were uncovered from near-field spectra (**Figure 2g**). On the other hand, fixed-wavelength near-field absorption imaging detected the spatial distribution of DNA and proteins in nuclear pores and interphase chromatin regions, respectively. The

authors also concluded that, compared to silicon wafers, gold-coated substrates are more suitable for s-SNOM imaging of cell nuclei due to the plasmonic enhancement.

s-SNOM provides unprecedented details in the characterization of tissue samples as well. Wiens et al. utilized s-SNOM to study damages induced in a bovine tail tendon by mechanical stress [80]. The submicron D-band pattern of collagen fibrils, a mesoscopic structure formed by intertwined helical collagens, was clearly resolved with ~67 nm spacing in near-field imaging (Figure 2h). Compared with polarization contrast FTIR imaging varying the polarization parallel to the sample plane, s-SNOM with vertically polarized light could extract additional information on the vertical alignment of the molecular orientation. Moreover, dentine, a dense, bony tissue beneath the enamel, was investigated by s-SNOM nearfield amplitude imaging [90]. The peritubular dentine and the intertubular dentine were clearly identified. In a different study, Stanciu et al. had explored the sample preparation protocols of zebrafish retinal tissue for correlative confocal laser scanning microscopy (CLSM) and s-SNOM imaging [91]. With proper treatments, the tissue sample was stained with fluorophores but still holds high transparency and flatness so that it was compatible with both CLSM and s-SNOM. At a home-built platform, the authors successfully obtained nanoscale s-SNOM images revealing a wealth of chemical details sectioned from small areas within microscale CLSM images. The integration of far-field microscopic method and near-field s-SNOM could aid the signal interpretation of s-SNOM and set an example for opportunities to enable a range of correlative studies combining powerful far-field LSM with s-SNOM.

3.4 s-SNOM in the characterization of biomolecules

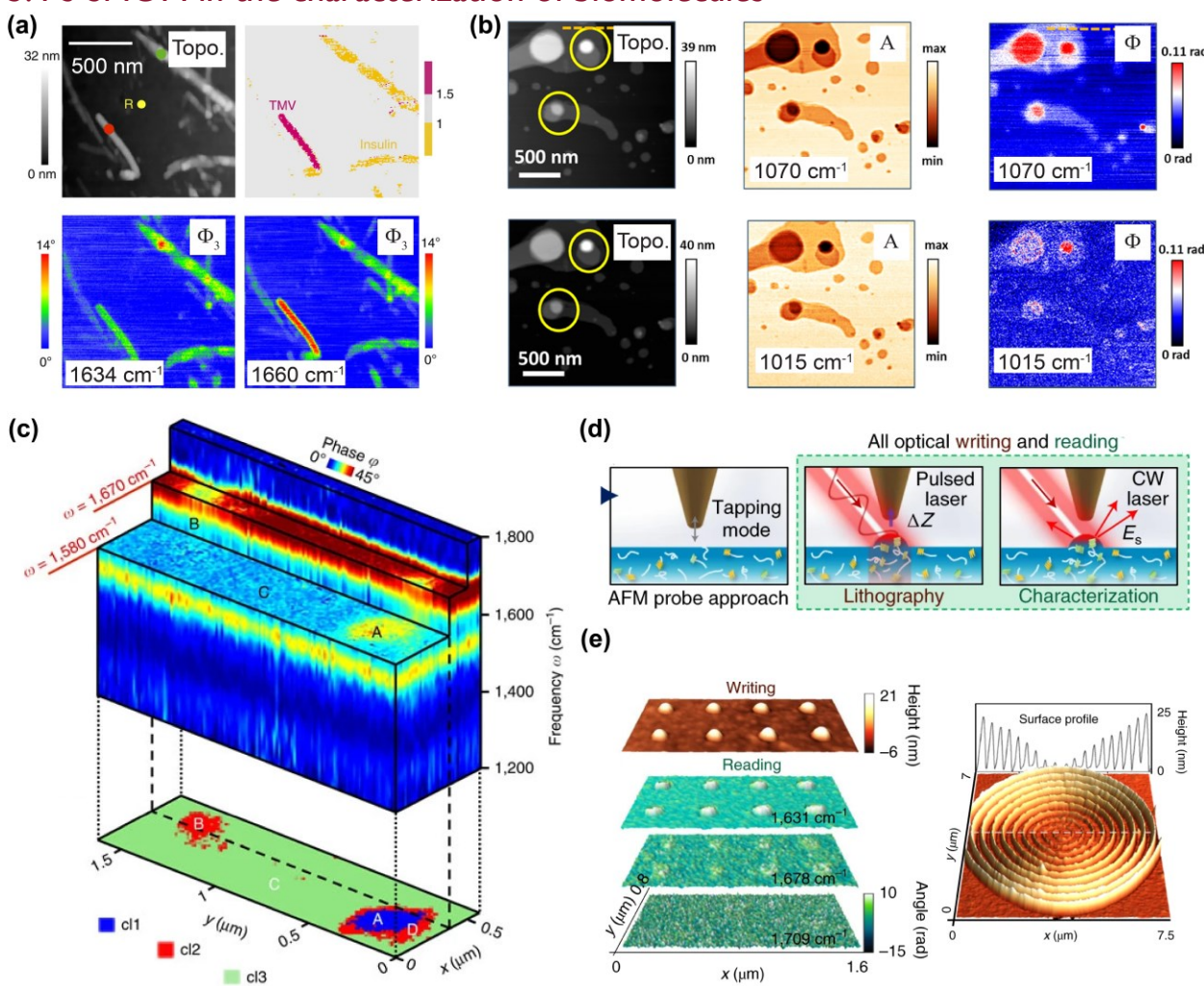


Figure 3. s-SNOM applications in biomolecules and biomaterial engineering. (a) AFM topography, composition map, s-SNOM phase (absorption) images at 1634 cm⁻¹ (β-sheet) and 1660 cm⁻¹ (α -helix). Based on s-SNOM absorption maps, a single TMV is identified from the mixture of insulin aggregates. Adapted from ref. [74] with permission. (b) AFM topography and s-SNOM amplitude (reflectivity) and phase (absorption) images at 1070 cm⁻¹ (C-O-P phosphate ester bond) and 1015 cm⁻¹ (background) of bilayers of DPPC. Adapted from ref. [92] with permission. (c) s-SNOM hyperspectral absorption imaging of the human hair cross-section. The data cube is sectioned at 1580 cm⁻¹ (amide II) and 1670 cm⁻¹ (amide I), revealing two nanopore structures (labeled with A and B). The cluster map obtained from the multivariate analysis is plotted at the bottom, indicating nanopore A contains melanin. In contrast, nanopore B could be either subsurface melanin or a thin slice of melanin granule. The ring structure (D) surrounding A is the interface between keratin and melanin. Adapted from ref. [93] with permission. (d) Schematics of tipenhanced near-field IR lithography based on s-SNOM. (e) Left panel: An example of written nano dots and reading the pattern at different IR frequencies. Right panel: A nanoscale spiral pattern written by the near-field IR lithography on silk proteins. The elevation of the feature height from center to peripheral is realized by increasing the IR power. (d) & (e) are adapted from ref. [94] with permission.

Biomolecules compose the most fundamental level of the hierarchical biological system. Since the development of nano-FTIR, s-SNOM has shown great potential in investigating biomolecules at the molecular level, whereas other optical methods lack the needed spatial resolution. Owing to large IR crosssections of protein amide bonds, nanostructures of proteins are among the first biomolecules investigated by s-SNOM. In 2011, Paulite et al. imaged individual β₂-microglobulin amyloid fibrils with s-SNOM, where heterogenous compositions of protein secondary structures were located at the single fibril level [95]. Furthermore, s-SNOM imaging and nano-FTIR have been utilized to characterize inclusion bodies induced by screened aggregating sequences in E. coli [96], revealing more β-sheet structures in inclusion bodies than in the cytoplasm. Similarly, nanoscale protein structures including ferritin complexes, bacteriorhodopsin on purple membranes, insulin aggregates, and amyloid-like insulin fibrils were investigated and benchmarked with s-SNOM [74]. Based on different IR signatures of α-helix and β-sheet, s-SNOM nano-FTIR was able to pinpoint individual TMVs mixed in insulin aggregates (Figure 3a) and reveal the presence of α -helices in the shell of insulin fibrils with < 10 nm thickness. Amelogenin is the major protein responsible for guiding the organization of apatite crystals in mature enamel. In a study conducted by Carneiro et al., s-SNOM was used to map self-assembled amyloid-like ribbons formed from amelogenin mimicking peptides with an amyloid-like motif [97]. Similarly, s-SNOM images of another type of mimicking peptides confirmed the presence of rich β -sheet contents within formed nanoribbons [98]. These findings at the nanoscale could help bridge the knowledge gap between the structure of amelogenin and the formation of enamel matrices during the biomineralization process.

Due to its superb surface sensitivity, s-SNOM is a suitable tool for characterizing delicate biomembranes. For example, a nanoscale single phospholipid bilayer composed of 1,2-dipalmutiyl-sn-glycero-3-phosphocholine (DPPC) was successfully resolved using s-SNOM imaging by Cernescu *et al.* (**Figure 3b**) [92]. Nano-FTIR spectra from a 5-nm thick single bilayer indicated the presence of N-H, C-H, C-O, and P-O vibrations, comparable to those from ATR-FTIR measurements. In addition, since the light polarization is always perpendicular to the sample surface, the authors also confirmed that s-SNOM provided polarization-dependent spectra that rely on the molecular orientation of vibrational modes. In another work, a bio-mimic monolayer formed by deuterated 1,2-distearoyl-sn-glycero-3-phosphocholine (DSPC) was mixed with the antibiotic surfactin. s-SNOM was employed to spectrally resolve a transition area of the domain boundary of scattered DSPC monolayer [99]. By depositing the sample on the epitaxial graphene on a SiC substrate, the authors found that the near-field graphene plasmon map is a good indicator with enhanced image contrast at domain boundaries. In parallel, near-field spectroscopic visualization of cholesterol-rich domains at the bilayer of 1,2-dimyristoyl-sn-glycero-3-phosphocholine (DMPC) was conducted by s-SNOM [100]. Three nano domains with different cholesterol concentrations – phase-separated cholesterol-rich domains, cholesterol-poor DMPC bilayer, and cholesterol-rich DMPC bilayer,

were discovered, confirming the optimal mixture ratio of cholesterol/DMPC to be 15/85. The -OH moiety of cholesterol was unveiled to spatially associated with ester groups of DMPC, suggesting the existence of hydrogen bonding between the two.

Several other small biomolecules were investigated by s-SNOM as well. In 2002, the monolayer sensitivity of s-SNOM had been demonstrated by Akhremitchev *et al.* on stamped DNA stripes with a thickness of 2 nm. Piccirilli *et al.* investigated the feasibility of carrying DNA molecules onto clay nanotubes [101]. They used s-SNOM nano-FTIR to characterize the distribution of adsorbed DNA on halloysite nanotubes and found that the DNA undergoes a structural shift upon the adsorption. Melanin in hairs is another small biomolecule with distinct IR absorptions. Amenabar *et al.* first demonstrated *in situ* hyperspectral s-SNOM imaging of native melanin in human hair (**Figure 3c**) [93]. Near-field absorption spectra from nano-FTIR distinguished Keratin-rich matrix and melanin granules. The hyperspectral data cube was further processed by the multivariate analysis, enabling the identification of either subsurface melanin or a thin slice of melanin granule. Likewise, melanosomes from sheep hairs were examined using s-SNOM [102]. IR signatures of two pigments – eumelanin and pheomelanin, were successfully extracted from individual nanoscale melanosomes *in situ*, which avoids the harsh treatment used in traditional chemical extractive methods. Additionally, by examining amide I&II absorption spectra of human hair, s-SNOM was proposed to be a complimentary method to monitor the hair condition in the trial of plasma lice comb [103].

3.5 s-SNOM in assisting biomaterial engineering

Label-free analysis on nanoscale chemical compositions enables s-SNOM to be a powerful tool for biomaterial characterization. For instance, s-SNOM has been exploited to monitor the growth of zinc-substituted hydroxyapatite nanofilms [104]. The existence and absence of non-stoichiometric sites and heterogeneous crystalline states during the growth were uncovered from nano-FTIR spectra.

Silks are largely accessible biomaterials with excellent mechanical strength, flexibility, biocompatibility, and biodegradability [105, 106]. The knowledge of silk proteins structures at the nanoscale can deepen the understanding of the structure-property relation and facilitate silk-based biomaterial engineering toward practical biocompatible applications. To image nanostructures of silk proteins with nanoscale resolution, thin slices of silk samples were measured with s-SNOM [107, 108]. As expected, strong amide I&II absorptions were recovered in the near-field absorption spectra. Notably, s-SNOM has been utilized to map nanopatterns on the silk proteins induced by electron-beam lithography [109]. In another study, s-SNOM was used to image the micropatterns generated by UV-photolithography utilizing silk fibroin light chain as the resist [110], which provides a new route for the wafer-scale bio-patterning.

Not only as a characterization method, but s-SNOM can also directly participate in the nano-structuring of silk proteins. Based on s-SNOM, Lee *et al.* successfully made a rewritable optical storage medium from silk proteins through the tip-enhanced near-field IR nanolithography (**Figure 3d-e**) [94]. The topographical change on silk proteins could reach ~35 nm lateral resolution, increasing the storage capacity to ~ 64 GB/inch². The pattern from nanolithography could be resolved by s-SNOM *in situ* and be erased by tuning the laser power at various levels. Thus, the tip from s-SNOM acts as pen, eraser, and reader. This work highlights the full potential of s-SNOM in combination with nanolithography.

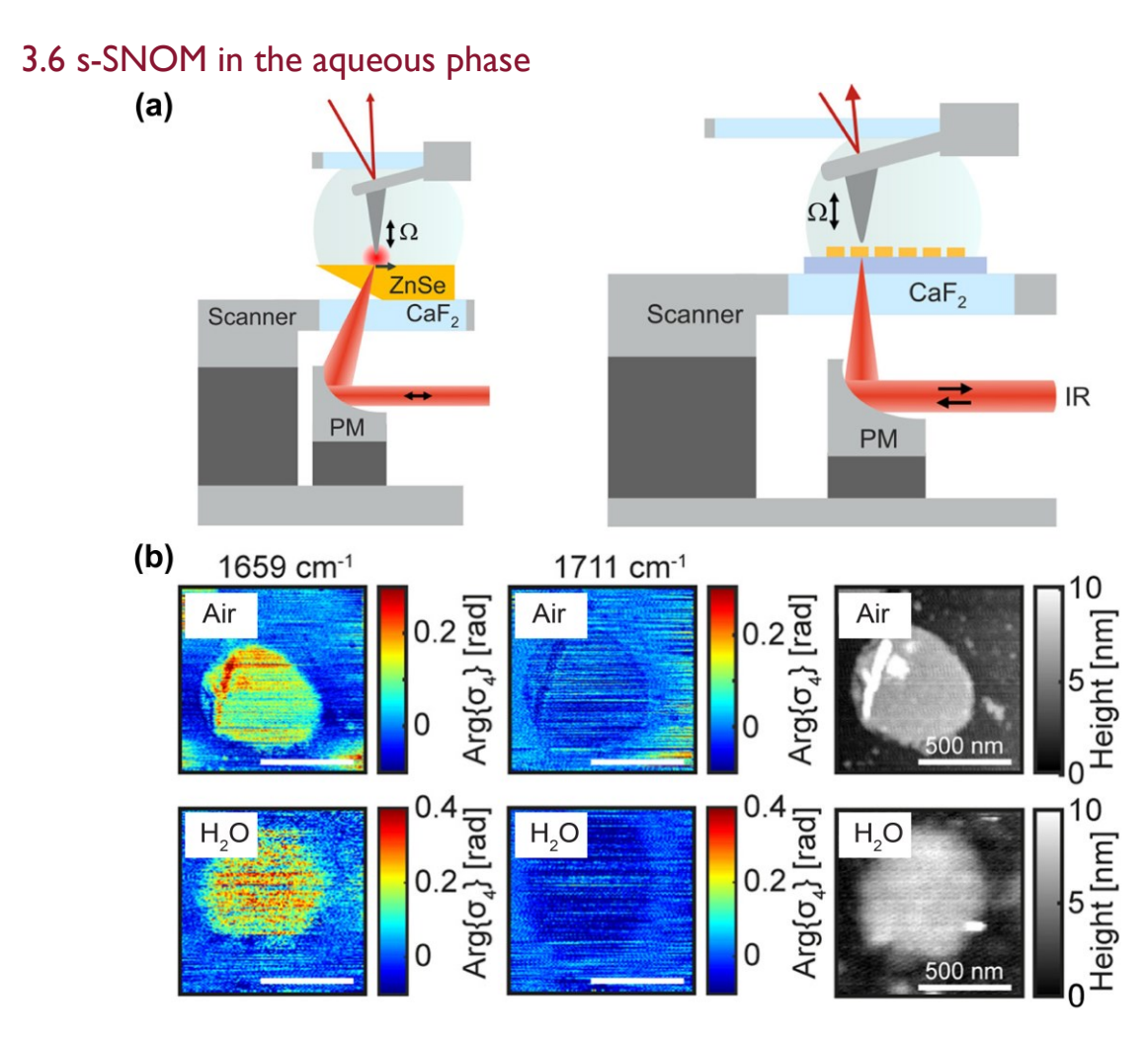


Figure 4. s-SNOM in water. (a) Generalized in-liquid s-SNOM setup with total internal reflection prism (left) or a simple IR-transparent window (right). Adapted from ref. [43] with permission. (b) s-SNOM images of the same patch of the purple membrane in air and water. Adapted from ref. [42] with permission.

Up until now, most s-SNOM applications in biological systems have been carried out in the air with dried specimens. This is because the IR light from the side illuminates the s-SNOM tip in free space in order to match the tip dipole polarization and avoid light blockage by the cantilever. This way, IR s-SNOM cannot

be easily implemented in water environments due to the strong water attenuation in mid-IR. However, a plethora of biological systems, such as cells and tissues, are functioning only in the aqueous environment. Therefore, it is imperative to investigate biological specimens in aqueous conditions with their native states and *in vivo*. To enable s-SNOM with the general in-liquid operation, a series of new configurations have been developed recently. These new configurations illuminate the tip-sample region from the bottom and employ an IR-transparent window or a total internal reflection prism/wedge as the substrate.

Utilizing the evanescent wave from total internal reflection on a ZnSe prism, O'Callahan *et al.* demonstrated s-SNOM in water. They used it to collect near-field phase spectra of catalase nanocrystals and biomimetic peptoid sheets with first harmonic demodulations [41]. Moreover, Pfitzner *et al.* took advantage of a silicon solid immersion lens and demonstrated s-SNOM imaging in water on purple membranes with second and third harmonic demodulations (**Figure 4b**) [42]. Later, Virmani *et al.* proposed a more general platform for in-liquid s-SNOM with either direct illumination through CaF₂ window or total internal reflection through ZnSe prism (**Figure 4a**) [43]. Such alignments allow for resolving both near-field amplitude and phase of phonon polaritons in background-free higher harmonic (2 – 4) demodulations. We foresee more high-resolution *in vivo* biological and pharmaceutical research to be realized by s-SNOM with the development of the liquid-phase operation.

3.7 PiFM in biological applications

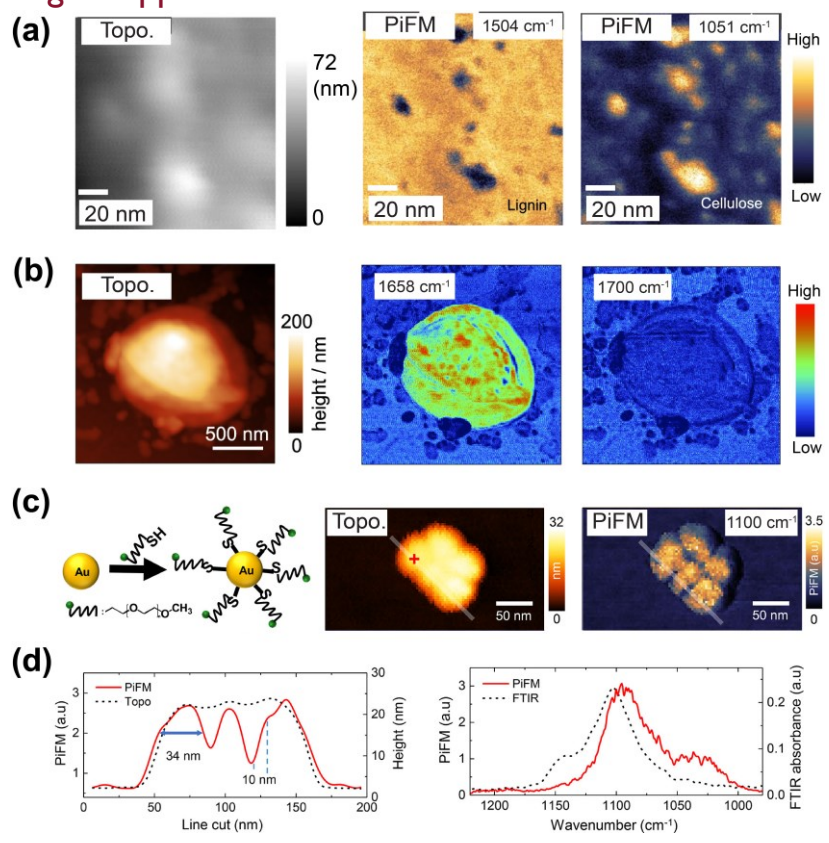


Figure 5. PiFM in biological applications. (a) AFM topography and PiFM images at 1504 cm⁻¹ (lignin absorption) and 1051 cm⁻¹ (cellulose absorption). The 1051 cm⁻¹ map shows cellulose enriched elementary fibrils (EFs). Adapted from ref. [111] with permission. (b) AFM Topography and PiFM images at 1658 cm⁻¹ (protein absorption) and 1700 cm⁻¹ (off-resonance) of bacterial cell walls of *Enterococcus faecium*. Adapted from ref. [112] with permission. (c) Left: A schematic of gold nanoparticles coated with monolayer poly(ethylene glycols) (PEGs). Middle and right: AFM topography and PiFM image at 1100 cm⁻¹ (PEG absorption) of a cluster of functionalized gold nanoparticles. (d) Left: Line-cut profiles along the white lines in topography and PiFM image in (b), indicating 10-nm spatial resolution. Right: PiFM spectrum collected from the red cross mark in the PiFM image overlapped with the bulk FTIR absorption spectrum of PEG functionalized gold nanoparticles. (c) & (d) are adapted from ref. [113] with permission.

As an emerging technique with the non-intrusive tapping mode operation, IR PiFM has also been implemented in analyzing biological specimens with nanoscale resolution. For instance, Kesari *et al.* utilized IR PiFM to investigate nanoscale heterogeneities of Norway spruce fiber wall [111]. On the ultrathin sample cross-section of the spruce, different cell wall layers were differentiated based on lignin and cellulose contents, and locations of small cellulose elementary fibrils (EFs) with widths of only 5 – 6 nm were identified in PiFM images (**Figure 5a**). In another study, Wang *et al.* mapped isolated bacterial cell walls of *Enterococcus faecium* with generalized heterodyne PiFM configuration (**Figure 5b**). Furthermore, PiFM was utilized to chemically map rod-shaped silica particles fabricated on the bio template of gene-modified *E. coli* [114]. The nanoscale spatial distribution of silica and proteins on the surface of bacteria was successfully revealed.

The excellent surface sensitivity and chemical specificity of PiFM have been reproduced on biomedical-related samples as well. As shown in **Figure 5c-d**, Jahng *et al.* demonstrated single-layer sensitivity with a 10-nm resolution of IR PiFM on 30-nm gold nanoparticles (AuNPs) functionalized with poly(ethylene glycols) (PEGs) [113]. As an extension of this capability, the authors also investigated magnetic AuNPs functionalized with dopamine-based tertiary amines. IR PiFM successfully revealed chemical contaminants on functionalized AuNPs on the single-particle level through the hyperspectral mapping, which could be easily omitted or undetectable in the ensemble FTIR. The high spatial resolution and monolayer sensitivity of IR PiFM enable it as a suitable tool in biomedical research, such as monitoring the quality of individual drug nanocarriers. For the detection of biotoxins, Ji *et al.* have established a platform based on IR PiFM to distinguish different biotoxins in a label-free manner [115]. In this study, PiFM spectra of toxin species were acquired at the single protein level. By applying the principal component analysis (PCA) to the obtained spectral data, a PCA identification database was set up and used to differentiate three major biotoxins, including abrin toxin, ricin toxin, and *Clostridium perfringens* exotoxin. With a similar strategy, PiFM has the potential to facilitate *in situ* biosensing research.

Like in-liquid s-SNOM, it is possible to implement PiFM in water with the total internal reflection configuration. However, the force heterodyne scheme of PiFM requires the cantilever to have high Q-factors for both mechanical resonances Ω_1 and Ω_2 , which is hard to fulfill in viscous liquid environments [116]. Recently, the first in-liquid operation of PiFM has been reported on the Au nano antenna [117]. With the development of a high-Q cantilever in liquid, it is expected that PiFM could be customized to be a nano-IR technique accommodating *in vivo* biological studies.

3.8 PFIR in biological applications

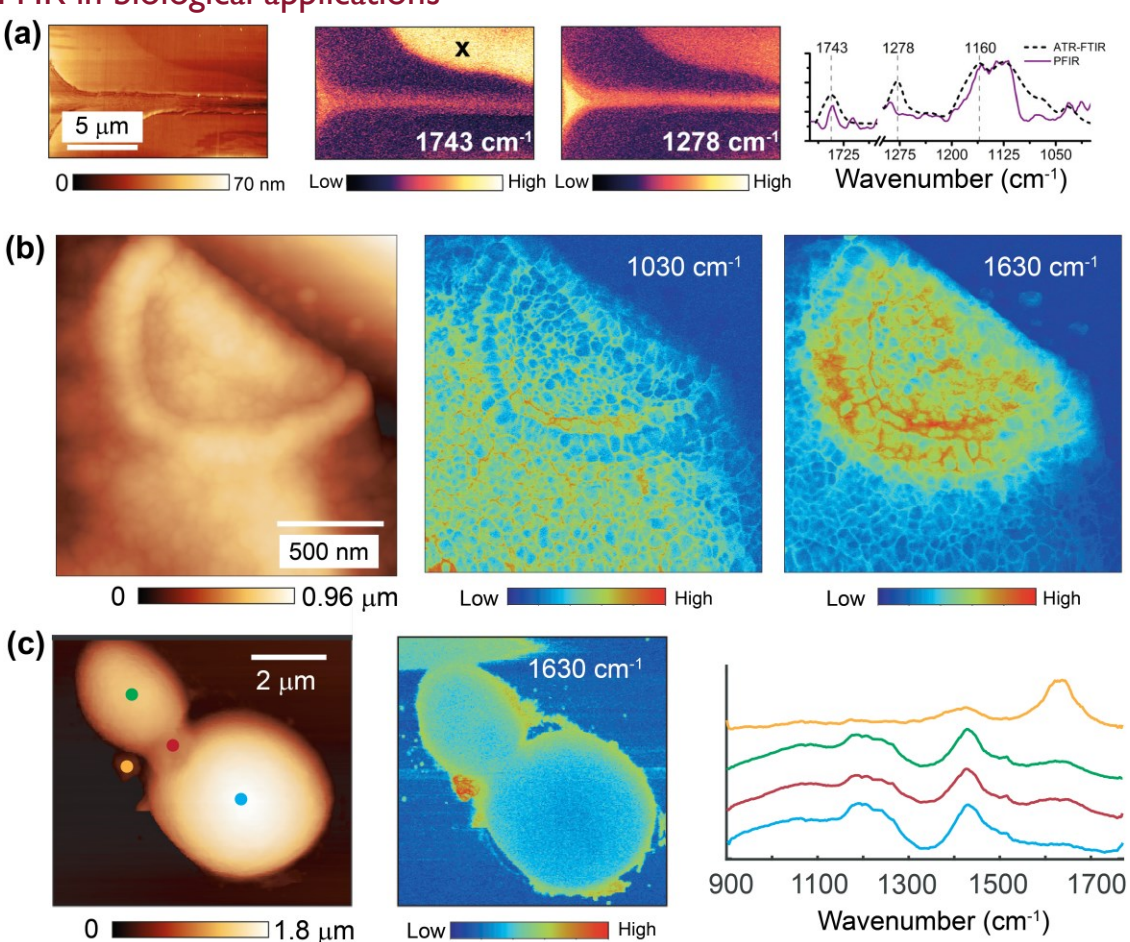


Figure 6. PFIR in the characterization of biological specimens. (a) AFM topography and PFIR images on polymerized wood cross-sections at 1743 cm⁻¹ (ester carbonyl) and 1278 cm⁻¹ (polymers C-F bonds and lignin). The rightmost panel shows the point PFIR spectrum collected from the cross mark in the 1743 cm⁻¹ image overlapped with the ATR-FTIR spectrum collected from the bulk. Adapted from ref. [67] with permission. (b) AFM topography and PFIR images at 1030 cm⁻¹ (polysaccharides) and 1630 cm⁻¹ (proteins and chitins) on the bud scar region of a dried zymosan particle. Adapted from ref. [66] with permission. (c) AFM topography and PFIR image at 1630 cm⁻¹ of two budding zymosan particles immersed in heavy water. The rightmost panel presents four point spectra collected from color-coded locations in the topography. The spectrum shown in yellow indicates the presence of proteins because of the strong amide I absorption between 1600 – 1700 cm⁻¹. Adapted from ref. [72] with permission.

PFT operation in commercial AFMs is well-tuned and calibrated, allowing for the accurate peak force control on the level from pico- to nano-Newton, which enables detecting samples with a variety of surface properties (e.g., hard, soft, and sticky) with a high spatial resolution [22, 59]. PFIR microscopy inherits the advantages from PFT and has been applied for multiple biological specimens. For example, Li *et al.* utilized PFIR microscopy to monitor the nanoscale quality of artificial phagocytic synapse nanoarrays [118]. As another example, Gusenbauer *et al.* used PFIR to reveal nanoscale chemical features of bio-based wooden matrices [67]. PFIR images and point spectra uncovered the chemical difference between the native and carboxylated wood sections. In addition, PFIR images and spectra at various nanoscale cell wall regions, including cell corner, secondary cell wall, polymerized cell wall, and middle lamella, unveiled distinct chemical compositions on each region (**Figure 6a**). In a parallel study, the surface chemistry of modified regenerated lignocellulose fibers were identified and verified with both chemical force microscopy (CFM) and multi-modal PFIR microscopy [119]. These results confirmed that in addition to traditional methods such as TEM and Raman microscopy, PFIR can provide a route to the routinely chemical characterization of the ultrastructure of lignocellulose materials.

In another study, PFIR imaging and spectroscopy helped uncover unprecedented structural details on zymosan particles derived from cell walls of *Saccharomyces cerevisiae* [66]. Zymosan particles belong to a group of natural immunomodulators applied in therapeutic applications [120-122]. PFIR images of zymosan particles showed the surface of the cell wall is enriched in polysaccharides, while the inner surface of bud scars is enriched with proteins and chitins. PFIR images with 6-nm spatial resolution around the bud scar revealed the mesh-like ultrastructure on the cell surface and the co-localization of proteins and polysaccharides (**Figure 6b**). Also, the combination of PFIR and super-resolution fluorescence microscopy allows visualizing the structural mechanism of β-glucans binding to their immune receptors.

The implementation of PFIR with the in-liquid operation (liquid-phase PFIR, or LiPFIR) was also successfully installed by Wang *et al.* with the total internal reflection geometry [65, 71, 72]. A spatial resolution of ~ 10 nm was demonstrated on protein fibrils in water [72]. Notably, the shape of immersed zymosan particles in water was very different from that in air, which underscores the necessity of characterizing biological specimens in their native states in water. Moreover, the modulus of zymosan particles in water drops to ~ 0.1 MPa. Samples with such high softness in water are still accessible by PFIR microscopy due to the precise force control of the PFT mode. By collecting IR absorption maps and point IR spectra from multiple locations, a protein cluster was found to be in proximity to the septum formed between two budding zymosan particles (**Figure 6c**). The protein cluster may mediate the chitin formation during the budding process [123]. The discovery enabled by PFIR is an example of how PFIR microscopy can help disentangle chemical structure-function relations at the fundamental level.

4. Summary and outlook

The spatial resolution of AFM-based nano-IR methods is no longer bound by the diffraction limit, but by the tip geometry and its curvature radius. Given the nanometer size of the metal-coated tip, the dimension of the tip-enhanced light field under far-field IR illumination is confined to a small tip-sample interaction region. All three reviewed techniques in this article – s-SNOM, PiFM, and PFIR take full advantage of the reduced tip-sample interaction region in non-contact tapping or PFT AFM operation, achieving 10 – 20 nm spatial resolutions on a routine basis without specialized AFM tips. In addition to the high spatial resolution, the strong near-field tip-enhancement also permits superb chemical sensitivity, as the monolayer sensitivity has already been demonstrated in both s-SNOM and PiFM. These features of AFM-based nano-IR techniques allow for the characterization of a broad spectrum of biological samples, yielding numerous discoveries with unprecedented details at the nanoscale. The involvement of s-SNOM, PiFM, and PFIR in biological research has dramatically expanded our scope of life-related mechanisms at the subcellular and the molecular level, which would accelerate the pace of biomaterial and pharmaceutical developments. As the in-liquid operation of s-SNOM, PiFM, and PFIR microscopy becomes mature, a number of fundamental biological and drug mechanisms are waiting to be explored.

However, the superb surface sensitivity of AFM-based nano-IR methods also limits their detection depth to only several tens of nanometers. For mammalian cell and hierarchical tissue samples, AFM-based techniques cannot easily obtain the much-desired spatial-temporal chemical information in all XYZ dimensions. The bulk sample could be microtomed into thin slices and then investigated by AFM layer by layer to address this challenge. The slice-and-view method has been employed in other surface-sensitive microscopies such as SEM to reveal ultrastructures of block copolymer [124]. In fact, several s-SNOM studies have already investigated slices microtomed from the bulk sample, such as hair [93], silk [108], and cellulose materials [125]. Recently, Kanevche *et al.* has reported s-SNOM imaging of 100 nm-thick cellular cross-sections of eukaryotic and prokaryotic cells, and a 3D tomogram with 20-nm IR resolution was composed [126]. The smooth combination of AFM-based nano-IR techniques with advanced microtome methodology will streamline the discovery of spatial-temporal correlations in life-relevant cells and tissues.

Although label-free chemical imaging is one of the attractive features of IR techniques, the integration of IR spectro-microscopy with small molecular tags usually yields higher molecular specificity and more meaningful metabolic information of biological systems. The metabolites labeled by IR-active probes can be pinpointed explicitly from complex cell backgrounds, where many intrinsic biomolecules share similar or overlapped IR signatures. For instance, based on distinct azide vibration in the cell silent region (1800 – 2600 cm⁻¹) and narrow bandwidth of specific chemical bonds (¹³C-edited carbonyl and deuterium-labeled bonds), a series of IR-active probe molecules were developed to track metabolic activities inside cells and

tissues *in situ* [127]. Such labeling strategy with small molecular tags and their distinct vibrational signatures from cell backgrounds have already been employed in Raman and coherent Raman microscopies [128, 129]. With the help of IR-active probe molecules, rich information of metabolic activities at the nanoscale will be extracted by tapping or peak force tapping AFM-based nano-IR techniques. Such information is imperative in unearthing fundamental mechanisms behind many physiological and pathological activities.

Furthermore, the incorporation of mid-IR spectro-microscopy with high-speed AFM (HS-AFM) may be a promising development. A short cantilever with much higher mechanical resonances (e.g., in MHz) is generally used in HS-AFM. HS-AFM can achieve a phenomenal imaging speed at tens of frames per second with proper cantilever Q-control, vibration suppression, and fast readout of the cantilever oscillation amplitude [130]. Such a high speed enables visualization of fast kinetics in cell biology [131], such as proteins walking along the actin filament [132]. Because HS-AFM uses tapping mode as well, s-SNOM and PiFM types of methodologies could be potentially integrated with HS-AFM operation, taking advantage of suitable laser sources, detectors, and improved signal acquisition speed. We anticipate that the video-rate chemical imaging of fast changes in physiological environments may be within reach in a not distant future.

Acknowledgments

H. W. thanks Dr. Qingyun Guo for helpful discussions. X.G.X would like to thank the support from the National Science Foundation CHE 1847765 and the support of the Beckman Young Investigator award from the Arnold and Mabel Beckman Foundation.

References

- [1] F. Hu, L. Shi, W. Min, Biological imaging of chemical bonds by stimulated Raman scattering microscopy, Nat. Methods, 16 (2019) 830-842, doi: 10.1038/s41592-019-0538-0.
- [2] Y. Shen, F. Hu, W. Min, Raman Imaging of Small Biomolecules, Annu. Rev. Biophys., 48 (2019) 347-369, doi: 10.1146/annurev-biophys-052118-115500.
- [3] B. Alberts, A. Johnson, J. Lewis, D. Morgan, M. Raff, P.W. Keith Roberts, Molecular biology of the cell, Garland Science, Taylor and Francis Group, New York, NY, 2015.
- [4] R. Yuste, Fluorescence microscopy today, Nat. Methods, 2 (2005) 902-904, doi: 10.1038/nmeth1205-902.
- [5] E. Abbe, Beiträge zur Theorie des Mikroskops und der mikroskopischen Wahrnehmung, Archiv für Mikroskopische Anatomie, 9 (1873) 413-468, doi: 10.1007/BF02956173.
- [6] E.H.K. Stelzer, Beyond the diffraction limit?, Nature, 417 (2002) 806-807, doi: 10.1038/417806a.
- [7] S.W. Hell, J. Wichmann, Breaking the diffraction resolution limit by stimulated emission: stimulated-emission-depletion fluorescence microscopy, Opt. Lett., 19 (1994) 780-782, doi: 10.1364/OL.19.000780.
- [8] E. Betzig, G.H. Patterson, R. Sougrat, O.W. Lindwasser, S. Olenych, J.S. Bonifacino, M.W. Davidson, J. Lippincott-Schwartz, H.F. Hess, Imaging Intracellular Fluorescent Proteins at Nanometer Resolution, Science, 313 (2006) 1642, doi: 10.1126/science.1127344.

- [9] M.J. Rust, M. Bates, X. Zhuang, Sub-diffraction-limit imaging by stochastic optical reconstruction microscopy (STORM), Nat. Methods, 3 (2006) 793-796, doi: 10.1038/nmeth929.
- [10] L.M. Ng, R. Simmons, Infrared Spectroscopy, Anal. Chem., 71 (1999) 343-350, doi: 10.1021/a1999908r.
- [11] S.G. Kazarian, K.L.A. Chan, ATR-FTIR spectroscopic imaging: recent advances and applications to biological systems, Analyst, 138 (2013) 1940-1951, doi: 10.1039/C3AN36865C.
- [12] D. Zhang, C. Li, C. Zhang, M.N. Slipchenko, G. Eakins, J.-X. Cheng, Depth-resolved mid-infrared photothermal imaging of living cells and organisms with submicrometer spatial resolution, Sci. Adv., 2 (2016) e1600521, doi: 10.1126/sciadv.1600521.
- [13] Z. Li, K. Aleshire, M. Kuno, G.V. Hartland, Super-Resolution Far-Field Infrared Imaging by Photothermal Heterodyne Imaging, J. Phys. Chem. B, 121 (2017) 8838-8846, doi: 10.1021/acs.jpcb.7b06065.
- [14] J. Shi, T.T.W. Wong, Y. He, L. Li, R. Zhang, C.S. Yung, J. Hwang, K. Maslov, L.V. Wang, High-resolution, high-contrast mid-infrared imaging of fresh biological samples with ultraviolet-localized photoacoustic microscopy, Nat. Photonics, 13 (2019) 609-615, doi: 10.1038/s41566-019-0441-3.
- [15] A. Centrone, Infrared Imaging and Spectroscopy Beyond the Diffraction Limit, Annu. Rev. Anal. Chem., 8 (2015) 101-126, doi: 10.1146/annurev-anchem-071114-040435.
- [16] A. Dazzi, C.B. Prater, AFM-IR: Technology and Applications in Nanoscale Infrared Spectroscopy and Chemical Imaging, Chem. Rev., 117 (2017) 5146-5173, doi: 10.1021/acs.chemrev.6b00448.
- [17] L. Xiao, Z.D. Schultz, Spectroscopic Imaging at the Nanoscale: Technologies and Recent Applications, Anal. Chem., 90 (2018) 440-458, doi: 10.1021/acs.analchem.7b04151.
- [18] D. Kurouski, A. Dazzi, R. Zenobi, A. Centrone, Infrared and Raman chemical imaging and spectroscopy at the nanoscale, Chem. Soc. Rev., 49 (2020) 3315-3347, doi: 10.1039/C8CS00916C.
- [19] L. Novotny, B. Hecht, Principles of Nano-Optics, Cambridge University Press, Cambridge, 2006.
- [20] A. Dazzi, R. Prazeres, F. Glotin, J.M. Ortega, Local infrared microspectroscopy with subwavelength spatial resolution with an atomic force microscope tip used as a photothermal sensor, Opt. Lett., 30 (2005) 2388-2390, doi: 10.1364/OL.30.002388.
- [21] D. Rugar, P. Hansma, Atomic Force Microscopy, Phys. Today, 43 (1990) 23-30, doi: 10.1063/1.881238.
- [22] B. Pittenger, N. Erina, C. Su, Quantitative mechanical property mapping at the nanoscale with PeakForce QNM, Application Note Veeco Instruments Inc, 1 (2010) 1-11, doi: N/A.
- [23] A. Rosa-Zeiser, E. Weilandt, S. Hild, O. Marti, The simultaneous measurement of elastic, electrostatic and adhesive properties by scanning force microscopy: pulsed-force mode operation, Meas. Sci. Technol., 8 (1997) 1333-1338, doi: 10.1088/0957-0233/8/11/020.
- [24] E. Meyer, H.J. Hug, R. Bennewitz, Scanning probe microscopy, Springer2003.
- [25] T. Hartmann, R. Gatz, W. Wiegräbe, A. Kramer, A. Hillebrand, K. Lieberman, W. Baumeister, R. Guckenberger, A Scanning Near-Field Optical Microscope (SNOM) for Biological Applications, in: D.W. Pohl, D. Courjon (Eds.) Near Field Optics, Springer Netherlands, Dordrecht, 1993, pp. 35-44.
- [26] V. Subramaniam, A.K. Kirsch, T.M. Jovin, Cell biological applications of scanning near-field optical microscopy (SNOM), Cell Mol Biol (Noisy-le-grand), 44 (1998) 689-700, doi: N/A.
- [27] D. Richards, A. Zayats, F. Keilmann, R. Hillenbrand, Near-field microscopy by elastic light scattering from a tip, Philos. Trans. R. Soc., A, 362 (2004) 787-805, doi: 10.1098/rsta.2003.1347.
- [28] A. Lahrech, R. Bachelot, P. Gleyzes, A.C. Boccara, Infrared-reflection-mode near-field microscopy using an apertureless probe with a resolution of $\lambda/600$, Opt. Lett., 21 (1996) 1315-1317, doi: 10.1364/OL.21.001315.
- [29] R. Bachelot, P. Gleyzes, A.C. Boccara, Near-field optical microscope based on local perturbation of a diffraction spot, Opt. Lett., 20 (1995) 1924-1926, doi: 10.1364/OL.20.001924.
- [30] B. Knoll, F. Keilmann, Near-field probing of vibrational absorption for chemical microscopy, Nature, 399 (1999) 134-137, doi: 10.1038/20154.

- [31] R. Hillenbrand, T. Taubner, F. Keilmann, Phonon-enhanced light–matter interaction at the nanometre scale, Nature, 418 (2002) 159-162, doi: 10.1038/nature00899.
- [32] M. Wagner, Z. Fei, A.S. McLeod, A.S. Rodin, W. Bao, E.G. Iwinski, Z. Zhao, M. Goldflam, M. Liu, G. Dominguez, M. Thiemens, M.M. Fogler, A.H. Castro Neto, C.N. Lau, S. Amarie, F. Keilmann, D.N. Basov, Ultrafast and Nanoscale Plasmonic Phenomena in Exfoliated Graphene Revealed by Infrared Pump—Probe Nanoscopy, Nano Lett., 14 (2014) 894-900, doi: 10.1021/nl4042577.
- [33] H. Wang, L. Wang, X.G. Xu, Scattering-type scanning near-field optical microscopy with low-repetition-rate pulsed light source through phase-domain sampling, Nat. Commun., 7 (2016) 13212, doi: 10.1038/ncomms13212.
- [34] X.G. Xu, L. Gilburd, G.C. Walker, Phase stabilized homodyne of infrared scattering type scanning near-field optical microscopy, Appl. Phys. Lett., 105 (2014) 263104, doi: 10.1063/1.4905207.
- [35] N. Ocelic, A. Huber, R. Hillenbrand, Pseudoheterodyne detection for background-free near-field spectroscopy, Appl. Phys. Lett., 89 (2006) 101124, doi: 10.1063/1.2348781.
- [36] L. Wang, X.G. Xu, Scattering-type scanning near-field optical microscopy with reconstruction of vertical interaction, Nat. Commun., 6 (2015) 8973, doi: 10.1038/ncomms9973.
- [37] H. Wang, L. Wang, D.S. Jakob, X.G. Xu, Mapping three-dimensional near-field responses with reconstruction scattering-type scanning near-field optical microscopy, AIP Adv., 7 (2017) 055118, doi: 10.1063/1.4984924.
- [38] D.N. Basov, M.M. Fogler, F.J. García de Abajo, Polaritons in van der Waals materials, Science, 354 (2016) aag1992, doi: 10.1126/science.aag1992.
- [39] X. Chen, D. Hu, R. Mescall, G. You, D.N. Basov, Q. Dai, M. Liu, Modern Scattering-Type Scanning Near-Field Optical Microscopy for Advanced Material Research, Adv. Mater., 31 (2019) 1804774, doi: 10.1002/adma.201804774.
- [40] F. Huth, A. Govyadinov, S. Amarie, W. Nuansing, F. Keilmann, R. Hillenbrand, Nano-FTIR Absorption Spectroscopy of Molecular Fingerprints at 20 nm Spatial Resolution, Nano Lett., 12 (2012) 3973-3978, doi: 10.1021/nl301159v.
- [41] B.T. O'Callahan, K.-D. Park, I.V. Novikova, T. Jian, C.-L. Chen, E.A. Muller, P.Z. El-Khoury, M.B. Raschke, A.S. Lea, In Liquid Infrared Scattering Scanning Near-Field Optical Microscopy for Chemical and Biological Nanoimaging, Nano Lett., 20 (2020) 4497-4504, doi: 10.1021/acs.nanolett.0c01291.
- [42] E. Pfitzner, J. Heberle, Infrared Scattering-Type Scanning Near-Field Optical Microscopy of Biomembranes in Water, J. Phys. Chem. Lett., 11 (2020) 8183-8188, doi: 10.1021/acs.jpclett.0c01769.
- [43] D. Virmani, A. Bylinkin, I. Dolado, E. Janzen, J.H. Edgar, R. Hillenbrand, Amplitude- and Phase-Resolved Infrared Nanoimaging and Nanospectroscopy of Polaritons in a Liquid Environment, Nano Lett., 21 (2021) 1360-1367, doi: 10.1021/acs.nanolett.0c04108.
- [44] D. Nowak, W. Morrison, H.K. Wickramasinghe, J. Jahng, E. Potma, L. Wan, R. Ruiz, T.R. Albrecht, K. Schmidt, J. Frommer, D.P. Sanders, S. Park, Nanoscale chemical imaging by photoinduced force microscopy, Sci. Adv., 2 (2016) e1501571, doi: 10.1126/sciadv.1501571.
- [45] M.T. Cuberes, H.E. Assender, G.A.D. Briggs, O.V. Kolosov, Heterodyne force microscopy of PMMA/rubber nanocomposites: nanomapping of viscoelastic response at ultrasonic frequencies, J. Phys. D: Appl. Phys., 33 (2000) 2347-2355, doi: 10.1088/0022-3727/33/19/301.
- [46] J. Li, J. Jahng, J. Pang, W. Morrison, J. Li, E.S. Lee, J.-J. Xu, H.-Y. Chen, X.-H. Xia, Tip-Enhanced Infrared Imaging with Sub-10 nm Resolution and Hypersensitivity, J. Phys. Chem. Lett., 11 (2020) 1697-1701, doi: 10.1021/acs.jpclett.0c00129.
- [47] I. Rajapaksa, K. Uenal, H.K. Wickramasinghe, Image force microscopy of molecular resonance: A microscope principle, Appl. Phys. Lett., 97 (2010) 073121, doi: 10.1063/1.3480608.
- [48] J. Jahng, D.A. Fishman, S. Park, D.B. Nowak, W.A. Morrison, H.K. Wickramasinghe, E.O. Potma, Linear and Nonlinear Optical Spectroscopy at the Nanoscale with Photoinduced Force Microscopy, Acc. Chem. Res., 48 (2015) 2671-2679, doi: 10.1021/acs.accounts.5b00327.

- [49] H.U. Yang, M.B. Raschke, Resonant optical gradient force interaction for nano-imaging and-spectroscopy, New J. Phys., 18 (2016) 053042, doi: 10.1088/1367-2630/18/5/053042.
- [50] J. Jahng, E.O. Potma, E.S. Lee, Tip-Enhanced Thermal Expansion Force for Nanoscale Chemical Imaging and Spectroscopy in Photoinduced Force Microscopy, Anal. Chem., 90 (2018) 11054-11061, doi: 10.1021/acs.analchem.8b02871.
- [51] L. Wang, H. Wang, D. Vezenov, X.G. Xu, Direct Measurement of Photoinduced Force for Nanoscale Infrared Spectroscopy and Chemical-Sensitive Imaging, J. Phys. Chem. C, 122 (2018) 23808-23813, doi: 10.1021/acs.jpcc.8b09107.
- [52] J. Jahng, E.O. Potma, E.S. Lee, Nanoscale spectroscopic origins of photoinduced tip—sample force in the midinfrared, Proc. Natl. Acad. Sci., 116 (2019) 26359, doi: 10.1073/pnas.1913729116.
- [53] J. Mathurin, E. Pancani, A. Deniset-Besseau, K. Kjoller, C.B. Prater, R. Gref, A. Dazzi, How to unravel the chemical structure and component localization of individual drug-loaded polymeric nanoparticles by using tapping AFM-IR, Analyst, 143 (2018) 5940-5949, doi: 10.1039/C8AN01239C.
- [54] M. Tuteja, M. Kang, C. Leal, A. Centrone, Nanoscale partitioning of paclitaxel in hybrid lipid—polymer membranes, Analyst, 143 (2018) 3808-3813, doi: 10.1039/C8AN00838H.
- [55] K. Wieland, G. Ramer, V.U. Weiss, G. Allmaier, B. Lendl, A. Centrone, Nanoscale chemical imaging of individual chemotherapeutic cytarabine-loaded liposomal nanocarriers, Nano Res., 12 (2019) 197-203, doi: 10.1007/s12274-018-2202-x.
- [56] N. Piergies, A. Dazzi, A. Deniset-Besseau, J. Mathurin, M. Oćwieja, C. Paluszkiewicz, W.M. Kwiatek, Nanoscale image of the drug/metal mono-layer interaction: Tapping AFM-IR investigations, Nano Res., 13 (2020) 1020-1028, doi: 10.1007/s12274-020-2738-4.
- [57] F. Rico, C. Su, S. Scheuring, Mechanical Mapping of Single Membrane Proteins at Submolecular Resolution, Nano Lett., 11 (2011) 3983-3986, doi: 10.1021/nl202351t.
- [58] M.E. Dokukin, I. Sokolov, Quantitative Mapping of the Elastic Modulus of Soft Materials with HarmoniX and PeakForce QNM AFM Modes, Langmuir, 28 (2012) 16060-16071, doi: 10.1021/la302706b. [59] B. Pittenger, N. Erina, C. Su, Mechanical property mapping at the nanoscale using PeakForce QNM scanning probe technique, Nanomechanical analysis of high performance materials, Springer2014, pp.
- [60] J. Hu, S. Chen, D. Huang, Y. Zhang, S. Lü, M. Long, Global mapping of live cell mechanical features using PeakForce QNM AFM, Biophys. Rep., 6 (2020) 9-18, doi: 10.1007/s41048-019-00103-9.

31-51.

- [61] M. Li, N. Xi, L. Liu, Peak force tapping atomic force microscopy for advancing cell and molecular biology, Nanoscale, 13 (2021) 8358-8375, doi: 10.1039/D1NR01303C.
- [62] L. Wang, H. Wang, M. Wagner, Y. Yan, D.S. Jakob, X.G. Xu, Nanoscale simultaneous chemical and mechanical imaging via peak force infrared microscopy, Sci. Adv., 3 (2017) e1700255, doi: 10.1126/sciadv.1700255.
- [63] L. Wang, M. Wagner, H. Wang, S. Pau-Sanchez, J. Li, J.H. Edgar, X.G. Xu, Revealing Phonon Polaritons in Hexagonal Boron Nitride by Multipulse Peak Force Infrared Microscopy, Adv. Opt. Mater., 8 (2020) 1901084, doi: 10.1002/adom.201901084.
- [64] L. Wang, D. Huang, C.K. Chan, Y.J. Li, X.G. Xu, Nanoscale spectroscopic and mechanical characterization of individual aerosol particles using peak force infrared microscopy, Chem. Commun., 53 (2017) 7397-7400, doi: 10.1039/C7CC02301D.
- [65] H. Wang, E. Janzen, L. Wang, J.H. Edgar, X.G. Xu, Probing Mid-Infrared Phonon Polaritons in the Aqueous Phase, Nano Lett., 20 (2020) 3986-3991, doi: 10.1021/acs.nanolett.0c01199.
- [66] W. Li, H. Wang, X.G. Xu, Y. Yu, Simultaneous Nanoscale Imaging of Chemical and Architectural Heterogeneity on Yeast Cell Wall Particles, Langmuir, 36 (2020) 6169-6177, doi: 10.1021/acs.langmuir.0c00627.

- [67] C. Gusenbauer, D.S. Jakob, X.G. Xu, D.V. Vezenov, É. Cabane, J. Konnerth, Nanoscale Chemical Features of the Natural Fibrous Material Wood, Biomacromolecules, 21 (2020) 4244-4252, doi: 10.1021/acs.biomac.0c01028.
- [68] D.S. Jakob, L. Wang, H. Wang, X.G. Xu, Spectro-Mechanical Characterizations of Kerogen Heterogeneity and Mechanical Properties of Source Rocks at 6 nm Spatial Resolution, Anal. Chem., 91 (2019) 8883-8890, doi: 10.1021/acs.analchem.9b00264.
- [69] D.S. Jakob, H. Wang, G. Zeng, D.E. Otzen, Y. Yan, X.G. Xu, Peak Force Infrared–Kelvin Probe Force Microscopy, Angew. Chem., Int. Ed., 59 (2020) 16083-16090, doi: 10.1002/anie.202004211.
- [70] N. Li, X. Niu, L. Li, H. Wang, Z. Huang, Y. Zhang, Y. Chen, X. Zhang, C. Zhu, H. Zai, Y. Bai, S. Ma, H. Liu, X. Liu, Z. Guo, G. Liu, R. Fan, H. Chen, J. Wang, Y. Lun, X. Wang, J. Hong, H. Xie, D.S. Jakob, X.G. Xu, Q. Chen, H. Zhou, Liquid medium annealing for fabricating durable perovskite solar cells with improved reproducibility, Science, 373 (2021) 561, doi: 10.1126/science.abh3884.
- [71] H. Wang, L. Wang, E. Janzen, J.H. Edgar, X.G. Xu, Total Internal Reflection Peak Force Infrared Microscopy, Anal. Chem., 93 (2021) 731-736, doi: 10.1021/acs.analchem.0c01176.
- [72] H. Wang, J.M. González-Fialkowski, W. Li, Q. Xie, Y. Yu, X.G. Xu, Liquid-Phase Peak Force Infrared Microscopy for Chemical Nanoimaging and Spectroscopy, Anal. Chem., 93 (2021) 3567-3575, doi: 10.1021/acs.analchem.0c05075.
- [73] A.M. Charrier, A.C. Normand, A. Passian, P. Schaefer, A.L. Lereu, In situ plant materials hyperspectral imaging by multimodal scattering near-field optical microscopy, Commun. Mater., 2 (2021) 59, doi: 10.1038/s43246-021-00166-7.
- [74] I. Amenabar, S. Poly, W. Nuansing, E.H. Hubrich, A.A. Govyadinov, F. Huth, R. Krutokhvostov, L. Zhang, M. Knez, J. Heberle, A.M. Bittner, R. Hillenbrand, Structural analysis and mapping of individual protein complexes by infrared nanospectroscopy, Nat. Commun., 4 (2013) 2890, doi: 10.1038/ncomms3890.
- [75] S. Gamage, M. Howard, H. Makita, B. Cross, G. Hastings, M. Luo, Y. Abate, Probing structural changes in single enveloped virus particles using nano-infrared spectroscopic imaging, PLoS One, 13 (2018) e0199112, doi: 10.1371/journal.pone.0199112.
- [76] O. Khatib, J.D. Wood, A.S. McLeod, M.D. Goldflam, M. Wagner, G.L. Damhorst, J.C. Koepke, G.P. Doidge, A. Rangarajan, R. Bashir, E. Pop, J.W. Lyding, M.H. Thiemens, F. Keilmann, D.N. Basov, Graphene-Based Platform for Infrared Near-Field Nanospectroscopy of Water and Biological Materials in an Aqueous Environment, ACS Nano, 9 (2015) 7968-7975, doi: 10.1021/acsnano.5b01184.
- [77] L.S. Mészáros, P. Ceccaldi, M. Lorenzi, H.J. Redman, E. Pfitzner, J. Heberle, M. Senger, S.T. Stripp, G. Berggren, Spectroscopic investigations under whole-cell conditions provide new insight into the metal hydride chemistry of [FeFe]-hydrogenase, Chem. Sci., 11 (2020) 4608-4617, doi: 10.1039/D0SC00512F.
- [78] H. Amrania, L. Drummond, R.C. Coombes, S. Shousha, L. Woodley-Barker, K. Weir, W. Hart, I. Carter, C.C. Phillips, New IR imaging modalities for cancer detection and for intra-cell chemical mapping with a sub-diffraction mid-IR s-SNOM, Faraday Discuss., 187 (2016) 539-553, doi: 10.1039/C5FD00150A.
- [79] G.C. Ajaezi, M. Eisele, F. Contu, S. Lal, A. Rangel-Pozzo, S. Mai, K.M. Gough, Near-field infrared nanospectroscopy and super-resolution fluorescence microscopy enable complementary nanoscale analyses of lymphocyte nuclei, Analyst, 143 (2018) 5926-5934, doi: 10.1039/C8AN01341A.
- [80] R. Wiens, C.R. Findlay, S.G. Baldwin, L. Kreplak, J.M. Lee, S.P. Veres, K.M. Gough, High spatial resolution (1.1 μ m and 20 nm) FTIR polarization contrast imaging reveals pre-rupture disorder in damaged tendon, Faraday Discuss., 187 (2016) 555-573, doi: 10.1039/C5FD00168D.
- [81] L. Pereira, D.N.A. Flores-Borges, P.R.L. Bittencourt, J.L.S. Mayer, E. Kiyota, P. Araújo, S. Jansen, R.O. Freitas, R.S. Oliveira, P. Mazzafera, Infrared Nanospectroscopy Reveals the Chemical Nature of Pit Membranes in Water-Conducting Cells of the Plant Xylem, Plant Physiol., 177 (2018) 1629-1638, doi: 10.1104/pp.18.00138.

- [82] V.M.R. Zancajo, T. Lindtner, M. Eisele, A.J. Huber, R. Elbaum, J. Kneipp, FTIR Nanospectroscopy Shows Molecular Structures of Plant Biominerals and Cell Walls, Anal. Chem., 92 (2020) 13694-13701, doi: 10.1021/acs.analchem.0c00271.
- [83] G. Bakir, B.E. Girouard, R.W. Johns, C.R.J. Findlay, H.A. Bechtel, M. Eisele, S.G.W. Kaminskyj, T.E.S. Dahms, K.M. Gough, Ultrastructural and SINS analysis of the cell wall integrity response of Aspergillus nidulans to the absence of galactofuranose, Analyst, 144 (2019) 928-934, doi: 10.1039/C8AN01591K.
- [84] M. Lucidi, D.E. Tranca, L. Nichele, D. Ünay, G.A. Stanciu, P. Visca, A.M. Holban, R. Hristu, G. Cincotti, S.G. Stanciu, SSNOMBACTER: A collection of scattering-type scanning near-field optical microscopy and atomic force microscopy images of bacterial cells, GigaScience, 9 (2020), doi: 10.1093/gigascience/giaa129.
- [85] G. Birarda, A. Delneri, C. Lagatolla, P. Parisse, P. Cescutti, L. Vaccari, R. Rizzo, Multi-technique microscopy investigation on bacterial biofilm matrices: a study on Klebsiella pneumoniae clinical strains, Anal. Bioanal. Chem., 411 (2019) 7315-7325, doi: 10.1007/s00216-019-02111-7.
- [86] D.E. Tranca, S.G. Stanciu, R. Hristu, B.M. Witgen, G.A. Stanciu, Nanoscale mapping of refractive index by using scattering-type scanning near-field optical microscopy, Nanomedicine: NBM, 14 (2018) 47-50, doi: 10.1016/j.nano.2017.08.016.
- [87] A. Blat, J. Dybas, M. Kaczmarska, K. Chrabaszcz, K. Bulat, R.B. Kostogrys, A. Cernescu, K. Malek, K.M. Marzec, An Analysis of Isolated and Intact RBC Membranes—A Comparison of a Semiquantitative Approach by Means of FTIR, Nano-FTIR, and Raman Spectroscopies, Anal. Chem., 91 (2019) 9867-9874, doi: 10.1021/acs.analchem.9b01536.
- [88] M.B. Raschke, C. Lienau, Apertureless near-field optical microscopy: Tip—sample coupling in elastic light scattering, Appl. Phys. Lett., 83 (2003) 5089-5091, doi: 10.1063/1.1632023.
- [89] A. Rygula, R.F. Fernandes, M. Grosicki, B. Kukla, P. Leszczenko, D. Augustynska, A. Cernescu, A. Dorosz, K. Malek, M. Baranska, Raman imaging highlights biochemical heterogeneity of human eosinophils versus human eosinophilic leukaemia cell line, Br. J. Haematol., 186 (2019) 685-694, doi: 10.1111/bjh.15971.
- [90] T. Sui, J. Dluhoš, T. Li, K. Zeng, A. Cernescu, G. Landini, A.M. Korsunsky, Structure-Function Correlative Microscopy of Peritubular and Intertubular Dentine, Materials, 11 (2018) 1493, doi: 10.3390/ma11091493.
- [91] S.G. Stanciu, D.E. Tranca, R. Hristu, G.A. Stanciu, Correlative imaging of biological tissues with apertureless scanning near-field optical microscopy and confocal laser scanning microscopy, Biomed. Opt. Express, 8 (2017) 5374-5383, doi: 10.1364/BOE.8.005374.
- [92] A. Cernescu, M. Szuwarzyński, U. Kwolek, P. Wydro, M. Kepczynski, S. Zapotoczny, M. Nowakowska, L. Quaroni, Label-Free Infrared Spectroscopy and Imaging of Single Phospholipid Bilayers with Nanoscale Resolution, Anal. Chem., 90 (2018) 10179-10186, doi: 10.1021/acs.analchem.8b00485.
- [93] I. Amenabar, S. Poly, M. Goikoetxea, W. Nuansing, P. Lasch, R. Hillenbrand, Hyperspectral infrared nanoimaging of organic samples based on Fourier transform infrared nanospectroscopy, Nat. Commun., 8 (2017) 14402, doi: 10.1038/ncomms14402.
- [94] W. Lee, Z. Zhou, X. Chen, N. Qin, J. Jiang, K. Liu, M. Liu, T.H. Tao, W. Li, A rewritable optical storage medium of silk proteins using near-field nano-optics, Nat. Nanotechnol., 15 (2020) 941-947, doi: 10.1038/s41565-020-0755-9.
- [95] M. Paulite, Z. Fakhraai, I.T.S. Li, N. Gunari, A.E. Tanur, G.C. Walker, Imaging Secondary Structure of Individual Amyloid Fibrils of a β2-Microglobulin Fragment Using Near-Field Infrared Spectroscopy, J. Am. Chem. Soc., 133 (2011) 7376-7383, doi: 10.1021/ja109316p.
- [96] L. Khodaparast, L. Khodaparast, R. Gallardo, N.N. Louros, E. Michiels, R. Ramakrishnan, M. Ramakers, F. Claes, L. Young, M. Shahrooei, H. Wilkinson, M. Desager, W. Mengistu Tadesse, K.P.R. Nilsson, P. Hammarström, A. Aertsen, S. Carpentier, J. Van Eldere, F. Rousseau, J. Schymkowitz, Aggregating sequences that occur in many proteins constitute weak spots of bacterial proteostasis, Nat. Commun., 9 (2018) 866, doi: 10.1038/s41467-018-03131-0.

- [97] K.M.M. Carneiro, H. Zhai, L. Zhu, J.A. Horst, M. Sitlin, M. Nguyen, M. Wagner, C. Simpliciano, M. Milder, C.-L. Chen, P. Ashby, J. Bonde, W. Li, S. Habelitz, Amyloid-like ribbons of amelogenins in enamel mineralization, Scientific Reports, 6 (2016) 23105, doi: 10.1038/srep23105.
- [98] Y. Bai, Z. Yu, L. Ackerman, Y. Zhang, J. Bonde, W. Li, Y. Cheng, S. Habelitz, Protein nanoribbons template enamel mineralization, Proc. Natl. Acad. Sci., 117 (2020) 19201, doi: 10.1073/pnas.2007838117. [99] B. Kästner, C.M. Johnson, P. Hermann, M. Kruskopf, K. Pierz, A. Hoehl, A. Hornemann, G. Ulrich, J. Fehmel, P. Patoka, E. Rühl, G. Ulm, Infrared Nanospectroscopy of Phospholipid and Surfactin Monolayer Domains, ACS Omega, 3 (2018) 4141-4147, doi: 10.1021/acsomega.7b01931.
- [100] A.M. Siddiquee, A. Houri, K.A. Messalea, J. Lin, T. Daeneke, B. Abbey, A. Mechler, S. Kou, Nanoscale Probing of Cholesterol-Rich Domains in Single Bilayer Dimyristoyl-Phosphocholine Membranes Using Near-Field Spectroscopic Imaging, J. Phys. Chem. Lett., 11 (2020) 9476-9484, doi: 10.1021/acs.jpclett.0c02192.
- [101] F. Piccirilli, F. Tardani, A. D'Arco, G. Birarda, L. Vaccari, S. Sennato, S. Casciardi, S. Lupi, Infrared Nanospectroscopy Reveals DNA Structural Modifications upon Immobilization onto Clay Nanotubes, Nanomaterials, 11 (2021) 1103, doi: 10.3390/nano11051103.
- [102] V. Stanic, F.C.B. Maia, R.d.O. Freitas, F.E. Montoro, K. Evans-Lutterodt, The chemical fingerprint of hair melanosomes by infrared nano-spectroscopy, Nanoscale, 10 (2018) 14245-14253, doi: 10.1039/C8NR03146K.
- [103] L. Ten Bosch, A. Huber, P. Sauerbier, R. KÖHler, G. Avramidis, W. ViÖL, Effects of newly devised plasma lice comb on human hair, Plasma Sci. Technol., 21 (2019) 125502, doi: 10.1088/2058-6272/ab428b. [104] E.O. López, A.L. Rossi, P.L. Bernardo, R.O. Freitas, A. Mello, A.M. Rossi, Multiscale connections between morphology and chemistry in crystalline, zinc-substituted hydroxyapatite nanofilms designed for biomedical applications, Ceram. Int., 45 (2019) 793-804, doi: 10.1016/j.ceramint.2018.09.246.
- [105] C. Vepari, D.L. Kaplan, Silk as a biomaterial, Prog. Polym. Sci., 32 (2007) 991-1007, doi: 10.1016/j.progpolymsci.2007.05.013.
- [106] F.G. Omenetto, D.L. Kaplan, New Opportunities for an Ancient Material, Science, 329 (2010) 528, doi: 10.1126/science.1188936.
- [107] M. Ryu, R. Honda, A. Cernescu, A. Vailionis, A. Balčytis, J. Vongsvivut, J.-L. Li, D.P. Linklater, E.P. Ivanova, V. Mizeikis, Nanoscale optical and structural characterisation of silk, Beilstein J. Nanotechnol., 10 (2019) 922-929, doi: 10.3762/bjnano.10.93.
- [108] M. Ryu, R. Honda, A. Reich, A. Cernescu, J.-L. Li, J. Hu, S. Juodkazis, J. Morikawa, Near-Field IR Orientational Spectroscopy of Silk, Appl. Sci., 9 (2019), doi: 10.3390/app9193991.
- [109] N. Qin, S. Zhang, J. Jiang, S.G. Corder, Z. Qian, Z. Zhou, W. Lee, K. Liu, X. Wang, X. Li, Z. Shi, Y. Mao, H.A. Bechtel, M.C. Martin, X. Xia, B. Marelli, D.L. Kaplan, F.G. Omenetto, M. Liu, T.H. Tao, Nanoscale probing of electron-regulated structural transitions in silk proteins by near-field IR imaging and nanospectroscopy, Nat. Commun., 7 (2016) 13079, doi: 10.1038/ncomms13079.
- [110] W. Liu, Z. Zhou, S. Zhang, Z. Shi, J. Tabarini, W. Lee, Y. Zhang, S.N. Gilbert Corder, X. Li, F. Dong, L. Cheng, M. Liu, D.L. Kaplan, F.G. Omenetto, G. Zhang, Y. Mao, T.H. Tao, Precise Protein Photolithography (P3): High Performance Biopatterning Using Silk Fibroin Light Chain as the Resist, Adv. Sci., 4 (2017) 1700191, doi: 10.1002/advs.201700191.
- [111] K.K. Kesari, P. O'Reilly, J. Seitsonen, J. Ruokolainen, T. Vuorinen, Infrared photo-induced force microscopy unveils nanoscale features of Norway spruce fibre wall, Cellulose, 28 (2021) 7295-7309, doi: 10.1007/s10570-021-04006-2.
- [112] L. Wang, D.S. Jakob, H. Wang, A. Apostolos, M.M. Pires, X.G. Xu, Generalized Heterodyne Configurations for Photoinduced Force Microscopy, Anal. Chem., 91 (2019) 13251-13259, doi: 10.1021/acs.analchem.9b03712.

- [113] J. Jahng, J.G. Son, H. Kim, J. Park, T.G. Lee, E.S. Lee, Direct Chemical Imaging of Ligand-Functionalized Single Nanoparticles by Photoinduced Force Microscopy, J. Phys. Chem. Lett., 11 (2020) 5785-5791, doi: 10.1021/acs.jpclett.0c01536.
- [114] H. Ping, L. Poudel, H. Xie, W. Fang, Z. Zou, P. Zhai, W. Wagermaier, P. Fratzl, W. Wang, H. Wang, P. O'Reilly, W.-Y. Ching, Z. Fu, Synthesis of monodisperse rod-shaped silica particles through biotemplating of surface-functionalized bacteria, Nanoscale, 12 (2020) 8732-8741, doi: 10.1039/D0NR00669F.
- [115] B. Ji, A. Kenaan, S. Gao, J. Cheng, D. Cui, H. Yang, J. Wang, J. Song, Label-free detection of biotoxins via a photo-induced force infrared spectrum at the single-molecular level, Analyst, 144 (2019) 6108-6117, doi: 10.1039/C9AN01338E.
- [116] M. Jin, F. Lu, M.A. Belkin, High-sensitivity infrared vibrational nanospectroscopy in water, Light: Sci. Appl., 6 (2017) e17096-e17096, doi: 10.1038/lsa.2017.96.
- [117] J. Li, J. Pang, Z.-d. Yan, J. Jahng, J. Li, W. Morrison, J. Liang, Q.-Y. Zhang, X.-H. Xia, Antenna enhancing infrared photoinduced force imaging in aqueous environment with super-resolution and hypersensitivity, arXiv preprint, arXiv:2009.11555 (2020), doi: N/A.
- [118] M. Li, H. Wang, W. Li, X.G. Xu, Y. Yu, Macrophage activation on "phagocytic synapse" arrays: Spacing of nanoclustered ligands directs TLR1/2 signaling with an intrinsic limit, Sci. Adv., 6 (2020) eabc8482, doi: 10.1126/sciadv.abc8482.
- [119] C. Gusenbauer, T. Nypelö, D.S. Jakob, X.G. Xu, D.V. Vezenov, S. Asaadi, H. Sixta, J. Konnerth, Differences in surface chemistry of regenerated lignocellulose fibers determined by chemically sensitive scanning probe microscopy, Int. J. Biol. Macromol., 165 (2020) 2520-2527, doi: 10.1016/j.ijbiomac.2020.10.145.
- [120] M. Novak, V. Vetvicka, β -Glucans, History, and the Present: Immunomodulatory Aspects and Mechanisms of Action, J. Immunotoxicol., 5 (2008) 47-57, doi: 10.1080/15476910802019045.
- [121] R. De Smet, T. Demoor, S. Verschuere, M. Dullaers, G.R. Ostroff, G. Leclercq, L. Allais, C. Pilette, M. Dierendonck, B.G. De Geest, C.A. Cuvelier, β -Glucan microparticles are good candidates for mucosal antigen delivery in oral vaccination, J. Controlled Release, 172 (2013) 671-678, doi: 10.1016/j.jconrel.2013.09.007.
- [122] Y. Pan, X. Li, T. Kang, H. Meng, Z. Chen, L. Yang, Y. Wu, Y. Wei, M. Gou, Efficient delivery of antigen to DCs using yeast-derived microparticles, Scientific Reports, 5 (2015) 10687, doi: 10.1038/srep10687.
- [123] E. Cabib, A. Durán, Synthase III-dependent Chitin Is Bound to Different Acceptors Depending on Location on the Cell Wall of Budding Yeast, J. Biol. Chem., 280 (2005) 9170-9179, doi: 10.1074/jbc.M414005200.
- [124] X. Feng, C.J. Burke, M. Zhuo, H. Guo, K. Yang, A. Reddy, I. Prasad, R.-M. Ho, A. Avgeropoulos, G.M. Grason, E.L. Thomas, Seeing mesoatomic distortions in soft-matter crystals of a double-gyroid block copolymer, Nature, 575 (2019) 175-179, doi: 10.1038/s41586-019-1706-1.
- [125] Q. Zhu, R. Zhou, J. Liu, J. Sun, Q. Wang, Recent Progress on the Characterization of Cellulose Nanomaterials by Nanoscale Infrared Spectroscopy, Nanomaterials, 11 (2021), doi: 10.3390/nano11051353.
- [126] K. Katerina, B. David, E. Andreas, H. Pascal-Kolja, N. Dennis, H. Joachim, Infrared Nanoscopy and Tomography of Intracellular Structures, Research Square, (2021), doi: 10.21203/rs.3.rs-753486/v1.
- [127] L. Shi, X. Liu, L. Shi, H.T. Stinson, J. Rowlette, L.J. Kahl, C.R. Evans, C. Zheng, L.E.P. Dietrich, W. Min, Mid-infrared metabolic imaging with vibrational probes, Nat. Methods, 17 (2020) 844-851, doi: 10.1038/s41592-020-0883-z.
- [128] H. Yamakoshi, K. Dodo, A. Palonpon, J. Ando, K. Fujita, S. Kawata, M. Sodeoka, Alkyne-Tag Raman Imaging for Visualization of Mobile Small Molecules in Live Cells, J. Am. Chem. Soc., 134 (2012) 20681-20689, doi: 10.1021/ja308529n.
- [129] L. Wei, Z. Chen, L. Shi, R. Long, A.V. Anzalone, L. Zhang, F. Hu, R. Yuste, V.W. Cornish, W. Min, Supermultiplex vibrational imaging, Nature, 544 (2017) 465-470, doi: 10.1038/nature22051.

[130] T. Ando, T. Uchihashi, N. Kodera, High-Speed AFM and Applications to Biomolecular Systems, Annu. Rev. Biophys., 42 (2013) 393-414, doi: 10.1146/annurev-biophys-083012-130324.

[131] M. Shamir, Y. Bar-On, R. Phillips, R. Milo, SnapShot: Timescales in Cell Biology, Cell, 164 (2016) 1302-1302.e1301, doi: 10.1016/j.cell.2016.02.058.

[132] N. Kodera, D. Yamamoto, R. Ishikawa, T. Ando, Video imaging of walking myosin V by high-speed atomic force microscopy, Nature, 468 (2010) 72-76, doi: 10.1038/nature09450.